






# The Double Dust Envelopes of R Coronae Borealis Stars

Edward J. Montiel<sup>1,2</sup>, Geoffrey C. Clayton<sup>2</sup> , B. E. K. Sugerman<sup>3</sup>, A. Evans<sup>4</sup>, D. A. Garcia-Hernández<sup>5,6</sup>, N. Kameswara Rao<sup>7</sup> ,  
M. Matsuura<sup>8</sup> , and P. Tisserand<sup>9</sup>

<sup>1</sup> Physics Department, University of California, Davis, CA 95616, USA; [ejmontiel@ucdavis.edu](mailto:ejmontiel@ucdavis.edu)

<sup>2</sup> Department of Physics & Astronomy, Louisiana State University, Baton Rouge, LA 70803, USA

<sup>3</sup> Space Science Institute, 4750 Walnut St, Suite 205, Boulder, CO 80301, USA

<sup>4</sup> Astrophysics Group, Lennard Jones Laboratory, Keele University, Keele, Staffordshire, ST5 5BG, UK

<sup>5</sup> Instituto de Astrofísica de Canarias (IAC), E-38205 La Laguna, Tenerife, Spain

<sup>6</sup> Universidad de La Laguna (ULL), Departamento de Astrofísica, E-38206, La Laguna, Tenerife, Spain

<sup>7</sup> Indian Institute of Astrophysics, Koramangala II Block, Bangalore, 560034, India

<sup>8</sup> School of Physics and Astronomy, Cardiff University, Queens Buildings, The Parade, Cardiff, CF24 3AA, UK

<sup>9</sup> Sorbonne Universités, UPMC Univ Paris 6 et CNRS, UMR 7095, Institut d'Astrophysique de Paris, 98 bis bd Arago, F-75014 Paris, France

Received 2018 June 5; revised 2018 July 30; accepted 2018 July 30; published 2018 September 10

## Abstract

The study of extended, cold dust envelopes surrounding R Coronae Borealis (RCB) stars began with their discovery by the *Infrared Astronomical Satellite*. RCB stars are carbon-rich supergiants characterized by their extreme hydrogen deficiency and their irregular and spectacular declines in brightness (up to 9 mag). We have analyzed new and archival *Spitzer Space Telescope* and *Herschel Space Observatory* data of the envelopes of seven RCB stars to examine the morphology and investigate the origin of these dusty shells. *Herschel*, in particular, has revealed the first-ever bow shock associated with an RCB star with its observations of SU Tauri. These data have allowed the assembly of the most comprehensive spectral energy distributions (SEDs) of these stars with multiwavelength data from the ultraviolet to the submillimeter. Radiative transfer modeling of the SEDs implies that the RCB stars in this sample are surrounded by an inner warm (up to 1200 K) and an outer cold (up to 200 K) envelope. The outer shells are suggested to contain up to  $10^{-3} M_{\odot}$  of dust and have existed for up to  $10^5$  years depending on the expansion rate of the dust. This age limit indicates that these structures have most likely been formed during the RCB phase.

*Key words:* circumstellar matter – dust, extinction – stars: evolution – stars: mass loss

## 1. Introduction

R Coronae Borealis (RCB) stars provide an excellent opportunity to understand more about the advanced stages of stellar evolution (Clayton 1996, 2012). They form a rare class of hydrogen-poor, carbon-rich supergiants. Two formation scenarios have been proposed for their origin: the single-degenerate final helium-shell flash (FF) model and the double-degenerate (DD) white dwarf (WD) merger model (Iben et al. 1996; Saio & Jeffery 2002). The latter involves the merger of a CO and a He WD (Webbink 1984), while the former takes the hot, evolved central star of a planetary nebula (PN) and turns it into a cool supergiant (Fujimoto 1977; Renzini 1979).

The trademark behavior of RCB stars is their spectacular and irregular declines in brightness. These declines can take an RCB star up to 9 mag fainter than its peak brightness and are caused by the formation of discrete, thick clouds of carbon dust along the line of sight (Loreta 1935; O’Keefe 1939; Clayton 1996). All RCB stars show an infrared excess due to the presence of warm circumstellar material (CSM; Feast et al. 1997; Clayton 2012, and references therein). Further, some RCB stars have been found to have cold, extended nebulosity (e.g., Walker 1985, 1986; Schaefer 1986; Bright et al. 2011; Clayton et al. 2011a).

The origins of this CSM material as well as the progenitors of the central RCB stars still remain shrouded in mystery. One important difference between the RCB stars formed in the two scenarios is that in the FF model, they would be surrounded by a fossil neutral hydrogen-rich (H I-rich) PN shell (Walker 1985;

Gillett et al. 1986; Lawson et al. 1990; Clayton et al. 1999, 2011a). Three stars (Sakurai’s Object, V605 Aquilae, and FG Sagittae) have been observed to undergo FF outbursts that transformed them from hot, evolved stars into cool giants with spectroscopic properties similar to RCB stars (Clayton & De Marco 1997; Asplund et al. 1998, 1999, 2000; Gonzalez et al. 1998; Clayton et al. 2006). These FF stars are all surrounded by PNe that are still ionized. However, the cooler RCB central stars are no longer able to provide the needed ionizing radiation, so the atoms in the shell have recombined. The velocity of the fossil PN shell would be similar to its ejection velocity,  $\sim 20\text{--}30 \text{ km s}^{-1}$ .

In the DD scenario, the stars may have had PN phases, but they would have occurred so long ago,  $\sim 10^9$  years, that no structure resembling a fossil envelope would remain when the two WDs finally merge to form an RCB star. These shells could be material lost during the WD merger event itself. This would have happened much more recently,  $\lesssim 10^4$  years ago, and would imply these structures are much less massive than previously estimated (Gillett et al. 1986; Clayton et al. 2011a).

A third explanation for the observed shells is that they could have formed during the RCB phase. RCB stars are thought to produce dust at a rate of  $10^{-7}\text{--}10^{-6} M_{\odot} \text{ yr}^{-1}$  (Clayton 2012). Clayton et al. (2013a) have found that newly forming clouds are propelled away from the central star at speeds up to  $400 \text{ km s}^{-1}$ . This also could result in the observed envelopes on a timescale of about  $10^4$  years.

We are now in an era where high-spatial-resolution and high-sensitivity far-IR (FIR), submillimeter, and even radio observations

**Table 1**  
Stellar Properties and New Observations of Sample RCB and HdC Stars

Name	R.A. (J2000)	Decl. (J2000)	$[m_V]_{\max}$	$D_{\text{Modeled}}$ (kpc)	$D_{\text{Gaia}}$ (kpc)	$L_{\text{Modeled}}$ ( $L_{\odot}$ )	$T_{\text{eff}}$ (K)	Observations <sup>a</sup>
MV Sgr	18:44:31.97	-20:57:12.77	12.0	11.5	$9.14^{+275.0}_{-4.50}$	5200	16000	M
R CrB	15:48:34.41	+28:09:24.26	5.8	1.40	$1.31^{+0.24}_{-0.18}$	9150	6750	P
RY Sgr	19:16:32.76	-33:31:20.43	6.5	1.50	$1.97^{+0.54}_{-0.35}$	8900	7250	M,P,S
SU Tau	05:49:03.73	+19:04:22.00	9.5	3.30	$1.57^{+0.74}_{-0.38}$	10450	6500	M,P,S
UW Cen	12:43:17.18	-54:31:40.72	9.6	3.50	$7.28^{+25.8}_{-3.19}$	7320	7500	M,P
V854 Cen	14:34:49.41	-39:33:19.18	7.0	2.28	... <sup>b</sup>	11760	6750	M
V CrA	18:47:32.30	-38:09:32.32	9.4	5.50	... <sup>b</sup>	6550	6250	M,P,S
HD 173409	18:46:26.63	-31:20:32.07	9.5	... <sup>c</sup>	$2.00^{+0.55}_{-0.33}$	... <sup>c</sup>	7000	P,S

**Notes.**

<sup>a</sup> M: MIPS; P: PACS; S: SPIRE.

<sup>b</sup> No parallax in the *Gaia* DR2.

<sup>c</sup> The HD 173409 SED was not modeled in this work (see Section 5.8.3).

exist of RCB stars that can be used to study their cold CSM material. We present unpublished *Spitzer* and *Herschel* observations of the RCB/HdC stars: MV Sagittarii (MV Sgr), R Coronae Borealis (R CrB), RY Sagittarii (RY Sgr), SU Tauri (SU Tau), UW Centauri (UW Cen), V854 Centuari (V854 Cen), V Coronae Australis (V CrA), and HD 173409. We have constructed multiwavelength data sets ranging from the ultraviolet (UV) to submillimeter in order to better determine the mass, size, and morphology of the diffuse material surrounding these RCB stars.

## 2. Observations

We have combined multiwavelength observations, which range from the UV to the submillimeter, in order to construct the most comprehensive spectral energy distributions (SEDs) of our sample RCB stars. SEDs for R CrB and V605 Aql have been published previously in Clayton et al. (2011a) and Clayton et al. (2013b), respectively. Stellar properties for our sample of RCB stars are presented in Table 1. Figures 1–4 show the light curves from the American Association of Variable Star Observers (AAVSO<sup>10</sup>) of our sample RCB stars with the epochs of the various observations that are included in our SED analysis marked.

### 2.1. Ultraviolet Spectra

Many of the RCB stars were observed with the *International Ultraviolet Explorer* (IUE). Archival IUE data from the long-wavelength spectrograph in the large-aperture mode of MV Sgr, UW Cen, RY Sgr, and V854 Cen were retrieved from the Barbara A. Mikulski Archive for Space Telescopes (MAST). The V854 Cen observation, LWP19951, was originally a part of the IUE program “RCMBW” (PI Barbara A. Whitney) and has been previously published in papers by Clayton et al. (1992b) and Lawson et al. (1999). RY Sgr, LWP30613, came from the IUE program “HERAH” (PI Albert V. Holm) and appeared in Holm (1999). The IUE observation of MV Sgr, LWR09008, came from Angelo Cassatella’s program, AC414. The spectrum was included in a publication by Jeffery (1995). Finally, the observation for UW Cen, LWR

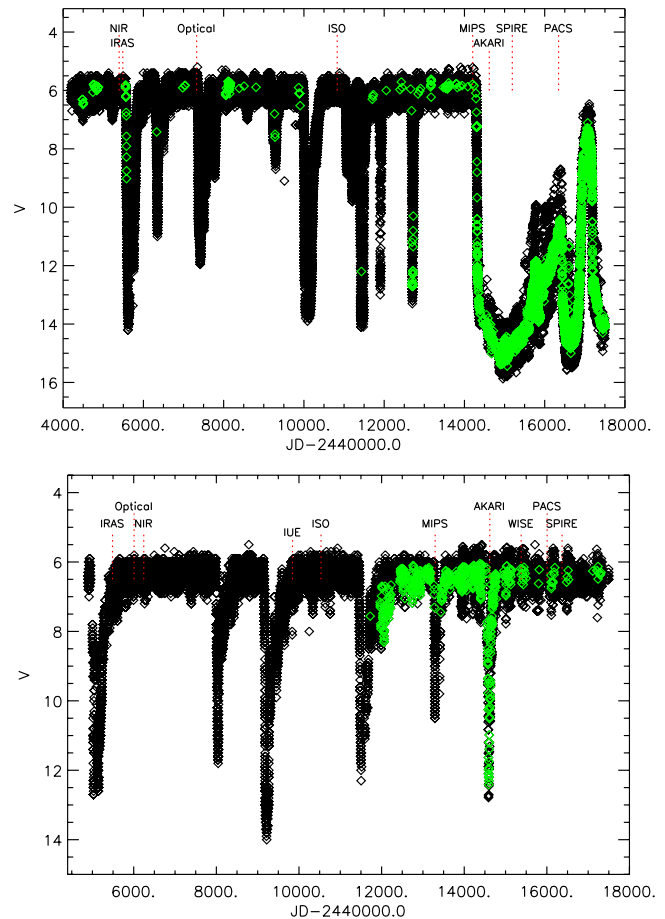


**Figure 1.** AAVSO observations of R CrB (top) and RY Sgr (bottom) since 1979 November and 1981 October, respectively. Black diamonds are visual observations, and green diamonds are Johnson V observations. The dates of the observations that went into the SED analysis are marked by the red, dashed vertical lines.

13260, originated in a program by Aneurin Evans (EC228). This spectrum has not appeared in any refereed publications. All IUE spectra were corrected using the IDL routine CCM\_UNRED, which applies correction as described by Cardelli et al. (1989).

<sup>10</sup> <https://www.aavso.org/data-download>

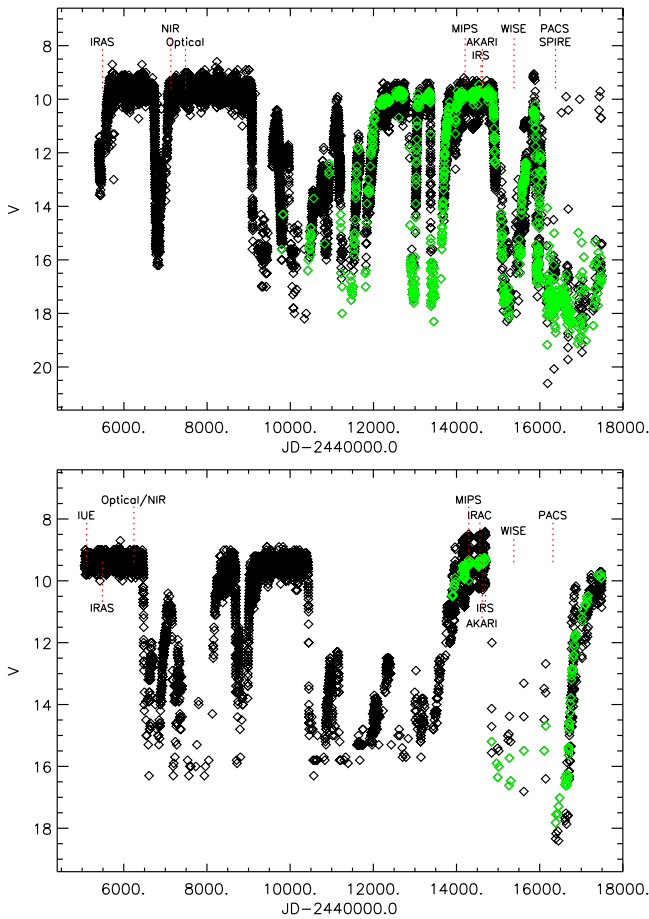


**Figure 2.** AAVSO observations of SU Tau (top) and UW Cen (bottom) since 1983 March and 1982 April, respectively. Black diamonds are visual observations, and green diamonds are Johnson  $V$  observations. The dates of the observations that went into the SED analysis are marked by the red, dashed vertical lines.

### 2.2. Optical Photometry

RCB stars have been observed at all states between maximum and minimum light. Extensive ground-based monitoring in the optical was performed by multiple groups during the last century. Maximum-light observations of SU Tau and V CrA were taken from Lawson et al. (1990). SU Tau was imaged in  $BVR_{C_I}$  photometric filters, while V CrA only in  $UBV$ . RY Sgr was observed near maximum light by Menzies & Feast (1997). They provide coverage with  $UBVR_{C_I}$  filters. Observations for MV Sgr and UW Cen at maximum light were retrieved from Goldsmith et al. (1990). They observed both RCB stars with  $UBVR_{C_I}$  filters. Maximum-light observations of V854 Cen were from Lawson & Cottrell (1989). The observations were performed with  $UBVR_{C_I}$  filters. HD 173409 is the only hydrogen-deficient (HdC) star, a type of star that is spectroscopically similar to RCB stars but has not been observed to have declines or an IR excess (see Section 5.8). Observations come from a monitoring campaign by Marang et al. (1990), who provide  $UBVR_{C_I}$  photometry. The photometry for our sample has been corrected for line-of-sight extinction by using the online<sup>11</sup> extinction calculator provided by the NASA/IPAC Extragalactic Database (NED) and the method of Schlafly & Finkbeiner (2011).

<sup>11</sup> <http://ned.ipac.caltech.edu/forms/calculator.html>

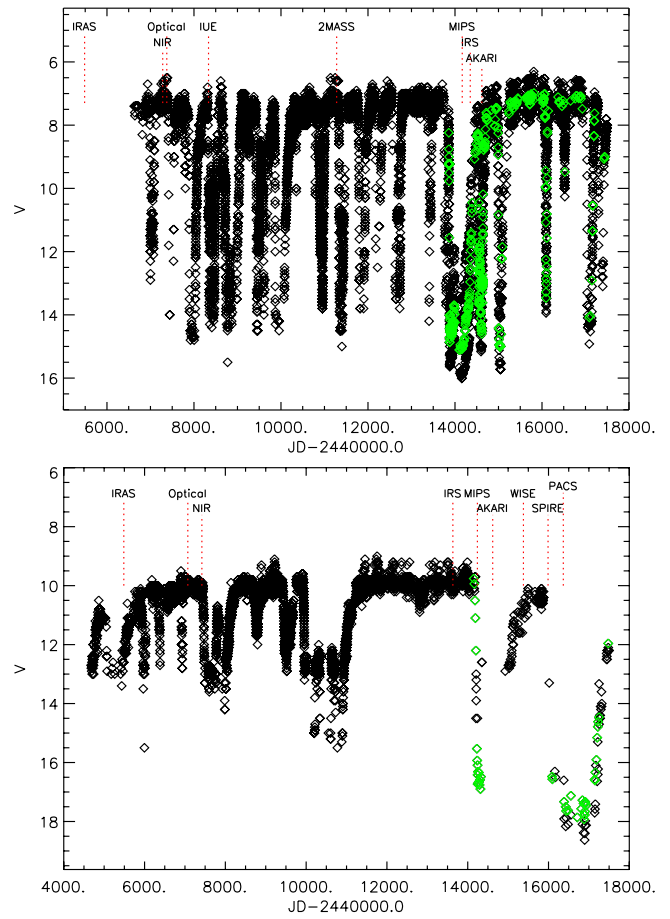


**Figure 3.** AAVSO observations of V854 Cen (top) and V CrA (bottom) since 1986 July and 1979 November, respectively. Black diamonds are visual observations, and green diamonds are Johnson  $V$  observations. The dates of the observations that went into the SED analysis are marked by the red, dashed vertical lines.

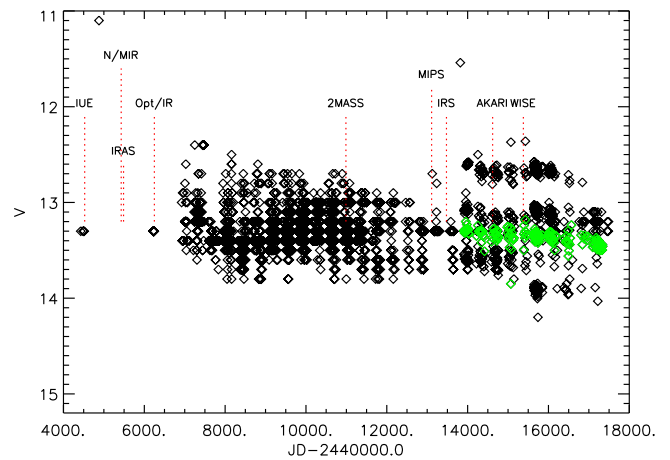


**Figure 4.** AAVSO observations of MV Sgr since 1980 October. Black diamonds are visual observations, and green diamonds are Johnson  $V$  observations. The times of the observations that went into the SED analysis are marked by the red, dashed vertical lines.

### 2.3. Near-infrared Photometry

Ground-based monitoring campaigns in the near-infrared (NIR), in the  $JHKLM$  bandpasses, have been conducted at a level similar to the optical.  $JH$  observations are primarily of the stellar photosphere, so they follow the fluctuations between

maximum and minimum light that distinguish the RCB class. *LM* track the warm dust that has recently formed around an RCB star, even if the dust is not in the line of sight.

NIR photometry for UW Cen also comes from Goldsmith et al. (1990), who also provided *MN* observations of MV Sgr. These observations were taken simultaneously with their optical campaign described in the previous section. *JHKLMN* observations from Kilkenny & Whittet (1984) were used for MV Sgr as well. Long-term NIR monitoring of HD 173409, RY Sgr, SU Tau, V854 Cen, and V CrA was reported by Feast et al. (1997) with photometry selected while the stars were at or near maximum light (see Figures 1–4). Additionally, photometry provided by the Two Micron All Sky Survey (2MASS; Skrutskie et al. 2006) was used if the RCB star was at maximum light during observation by the survey. This applied to only two RCB stars in the sample, MV Sgr and V854 Cen, as well as the HdC star, HD 173409. The photometry was taken from the 2MASS Point Source Catalog (Cutri et al. 2003).

#### 2.4. Infrared Space Observatory

The *Infrared Space Observatory (ISO)* was a joint European Space Agency (ESA), Japanese Aerospace Exploration Agency (JAXA), and NASA mission launched 1995 November 17. One of its instruments, the Short Wave Spectrometer (SWS; Leech et al. 2003), provided spectroscopy between 2.4 and 45  $\mu\text{m}$ . Calibrated SWS spectra of RY Sgr and R CrB (Sloan et al. 2003) were retrieved from an *ISO* SWS science archive hosted by Gregory C. Sloan.<sup>12</sup>

#### 2.5. Spitzer Space Telescope

*Spitzer Space Telescope (Spitzer)*; Rieke et al. 2004) observations of RCB stars were acquired with all three instruments on board the satellite. These instruments are the Infrared Array Camera (IRAC; Fazio et al. 2004), the Infrared Spectrograph (IRS; Houck et al. 2004), and the Multiband Imaging Photometer for *Spitzer* (MIPS; Rieke et al. 2004). IRAC was the NIR imager on *Spitzer* and provided simultaneous observations at 3.6, 4.5, 5.8, and 8.0  $\mu\text{m}$  (central wavelengths). Only UW Cen was observed with IRAC (PI A. Evans, ID 40061).

IRS provided wavelength coverage in the range 5.3–38  $\mu\text{m}$  with both low ( $R \sim 90$ ) and high ( $R \sim 600$ ) resolution (Houck et al. 2004). Archival IRS observations of RCB stars at both resolutions (PI D. Lambert, ID 50212) were previously published by García-Hernández et al. (2011b, 2013). Low-resolution IRS observations were retrieved from the Cornell Atlas of *Spitzer*/IRS Sources (CASSIS; Lebouteiller et al. 2011), which provides a standard reduction of all of the sources observed with the IRS. This was performed using the Spectroscopy Modeling Analysis and Reduction Tool (SMART; Higdon et al. 2004; Lebouteiller et al. 2010).

MIPS was the FIR imager on *Spitzer* and observed at (central) wavelengths of 24, 70, and 160  $\mu\text{m}$  with point-spread function (PSF) FWHMs of 6", 18", and 40", respectively. Archival MIPS observations of RCB stars come from two programs, PIs G. Clayton (ID 30029) and A. Evans (ID 3362). The raw data were processed using the MIPS DAT package (Gordon et al. 2005), which performs standard reductions for

IR array detectors as well as MIPS specific routines. The output images were then calibrated according to the methods established by Engelbracht et al. (2007), Gordon et al. (2007), and Stansberry et al. (2007) for the 24, 70, and 160  $\mu\text{m}$  bands, respectively.

#### 2.6. Wide-field Infrared Survey Explorer

The *Wide-field Infrared Survey Explorer (WISE)*; Wright et al. 2010) was a NASA medium-class explorer mission that was launched in 2009 December. Its mission was to survey the entire sky over 10 months at 3.4, 4.5, 12, and 22  $\mu\text{m}$ . Two catalogs of *WISE* sources were released in 2012 (*WISE All-Sky*; Cutri et al. 2012) and 2013 (*ALLWISE*; Cutri 2014), which encompass over 500 million and 700 million objects, respectively. The differences between the catalogs are detailed in Cutri (2014). We have adopted the *ALLWISE* photometry for our SED analysis, and this photometry can be found in the individual tables for our sample stars in Section 5. The *WISE* observations of R CrB and V854 Cen are saturated, which makes the published photometry in both catalogs unreliable and not usable.

#### 2.7. AKARI

*AKARI* was a JAXA satellite launched in 2006 February (Murakami et al. 2007) and operated in two modes: an all-sky survey, similar to *WISE*, and a pointed mode for specific targets. It had two instruments: the Infrared Camera (IRC; Onaka et al. 2007) and the Far Infrared Surveyor (FIS; Kawada et al. 2007). The IRC contained three individual cameras observing at central wavelengths of 3.6, 9, and 18  $\mu\text{m}$ . The FIS had two detector arrays that enabled both wide- and narrow-band FIR imaging. The central wavelengths of the narrow-band imaging were 65 and 160  $\mu\text{m}$ , while for wide-band imaging they were 90 and 140  $\mu\text{m}$ .

Two all-sky catalogs were released by the *AKARI* team. They are an MIR/IRC catalog (Ishihara et al. 2010), which published photometry at 9 or 18  $\mu\text{m}$  for  $\sim 870,000$  individual sources, and an FIR/FIS catalog (Yamamura et al. 2009) containing the four FIS bands for  $\sim 430,000$  sources. *AKARI* photometry, in at least one of the six bands, was published for all of the RCB stars in our sample.

#### 2.8. Infrared Astronomical Satellite

The *Infrared Astronomical Satellite (IRAS)*; Neugebauer et al. 1984), which was the first space-based observatory to survey the entire sky in the IR, operated in the MIR and FIR at central wavelengths of 12, 25, 60, and 100  $\mu\text{m}$ . Two catalogs of *IRAS* photometry have been published and updated since the end of the mission. They are the *IRAS Faint Source Catalog (FSC)*; Moshir et al. 1990) and the Point Source Catalog (PSC; Helou & Walker 1988). Both catalogs provide photometry in at least one of the four *IRAS* bands for a total of  $\sim 300,000$  individual sources. All of the RCB stars in our sample have *IRAS* observations in at least one of the four bands.

#### 2.9. Herschel Space Observatory

The *Herschel Space Observatory (Herschel)*; Pilbratt et al. 2010) has allowed for improved space-based resolution in both the FIR and submillimeter to detect and map cold dust surrounding stars. Our sample of RCB stars was observed with *Herschel* under an open time program led by PI G. Clayton (OT1\_gclayton\_1; 25.6 hr). Observations were conducted

<sup>12</sup> <https://isc.astro.cornell.edu/sloan/library/swsatlas/aot1.html>

with both the Photodetector Array Camera and Spectrometer (PACS) at 70, 100, and 160  $\mu\text{m}$  (Poglitsch et al. 2010) and the Spectral and Photometric Imaging REceiver (SPIRE) at 250, 350, and 500  $\mu\text{m}$  (Griffin et al. 2010).

The IDL routine Scanamorphos (version 21.0; Roussel 2013) was used to generate all of the final PACS and SPIRE maps for analysis. The map-making process begins by downloading the raw satellite telemetry (Level 0 products) from the *Herschel* Science Archive. These products are then converted to physical units (Level 1 products), such as temperatures or voltages, with the *Herschel* Interactive Processing Environment (HIPE, version 12, Ott 2010). HIPE is both a GUI and command-line-based software written in Jython (Java+Python). It is at these Level 1 products where the typical HIPE pipeline is interrupted (further processing with HIPE all the way to image products is possible) to generate FITS binary files that *Scanamorphos* can read and interact with. PACS maps are generated in the units of  $\text{Jy pixel}^{-1}$  with  $1''0$ ,  $1''4$ , and  $2''0$  pixels at 70, 100, and 160  $\mu\text{m}$ , respectively. The choice of these pixel sizes corresponds to PSFs with FWHMs of, in increasing wavelength,  $6''$ ,  $7''$ , and  $11''$ . SPIRE maps are generated in units of  $\text{Jy beam}^{-1}$  and are then converted into  $\text{Jy pixel}^{-1}$  through a multiplicative constant derived from the individual SPIRE beams for each wavelength band. The maps have pixel sizes of  $6''0$ ,  $10''0$ , and  $14''0$  at 250, 350, and 500  $\mu\text{m}$ , respectively. The SPIRE PSFs have FWHM of, in increasing wavelength,  $18''$ ,  $24''$ , and  $37''$ .

### 3. Photometry

Photometry was done on the *Spitzer* and *Herschel* images in order to generate SEDs for the stars in our sample. Many different programs have been written to perform automated aperture and PSF photometry. We used the automated aperture routine Source Extractor (SExtractor; Bertin & Arnouts 1996). The power of SExtractor is in its many tunable parameters that allow the user to maximize the program to perform photometry on their desired objects, whether they be point source or extended. SExtractor also provides robust post-run ancillary products such as residual, background, object, and aperture images in addition to performing aperture photometry on any given input images. These diagnostics were used to judge the success of any run. Further, we chose to use the IDL routine StarFinder (Diolaiti et al. 2000a, 2000b), which performs PSF photometry. StarFinder, similar to SExtractor, provides a suite of post-run images for the purpose of diagnostics. In particular, the point source subtracted image is of great use for investigating the presence of any faint nebulosity. SExtractor was used for all of the photometry except for the *Spitzer*/MIPS observations of V CrA, which are from StarFinder. The photometry used in this study for the individual stars is listed in Tables 2–10.

### 4. SED Modeling

#### 4.1. Monte Carlo Radiative Transfer

We performed Monte Carlo radiative transfer (MCRT) modeling of the SEDs for the stars in our sample to better constrain the morphology and physical parameters of the dust surrounding these objects. We used the fully 3D MOnTe CARlo SimulationS of Ionized Nebulae (MOCASSIN; version 2.02.70) code (Ercolano et al. 2003, 2005, 2008). The code is written in Fortran 90 and is capable of being run with parallel

**Table 2**  
MV Sgr Photometry

Band	Flux (Jy)	$\sigma$ (Jy)
<i>U</i> (0.365)	0.013	1.20e-04
<i>B</i> (0.433)	0.015	1.40e-04
<i>V</i> (0.550)	0.018	1.60e-04
<i>R<sub>C</sub></i> (0.640)	0.015	1.40e-04
<i>I<sub>C</sub></i> (0.790)	0.025	2.30e-04
2MASS/ <i>J</i> (1.235)	0.060	0.001
<i>J</i> (1.25)	0.075	0.007
<i>H</i> (1.60)	0.130	0.012
2MASS/ <i>H</i> (1.66)	0.117	0.003
2MASS/ <i>K<sub>S</sub></i> (2.16)	0.188	0.004
<i>K</i> (2.20)	0.213	0.020
<i>L</i> (3.40)	0.344	0.032
<i>WISE</i> /3.4	0.180	0.004
<i>WISE</i> /4.6	0.199	0.004
<i>M</i> (4.80)	0.874	0.402
<i>M</i> (4.80)	0.551	3 $\sigma$ upper limit
<i>AKARI</i> /9	0.330	0.019
<i>N</i> (10.2)	0.814	0.150
<i>N</i> (10.2)	0.742	0.068
<i>IRAS</i> /12	0.597	0.130
<i>WISE</i> /12	0.409	0.006
<i>AKARI</i> /18	1.00	0.008
<i>WISE</i> /22	1.11	0.017
<i>MIPS</i> /24	1.00	0.004
<i>IRAS</i> /25	1.57	0.140
<i>IRAS</i> /60	0.777	0.078
<i>AKARI</i> /65	0.257	3 $\sigma$ upper limit
<i>MIPS</i> /70	0.286	0.009
<i>AKARI</i> /90	0.496	0.103
<i>IRAS</i> /100	3.47	3 $\sigma$ upper limit

**Table 3**  
R CrB Photometry

Band	Flux (Jy)	$\sigma$ (Jy)
<i>U</i> (0.365)	4.53	0.039
<i>B</i> (0.433)	11.60	0.107
<i>V</i> (0.550)	17.90	0.166
<i>R<sub>C</sub></i> (0.640)	20.50	0.190
<i>I<sub>C</sub></i> (0.790)	20.70	0.191
<i>J</i> (1.25)	17.70	0.165
<i>H</i> (1.60)	14.30	0.100
<i>K</i> (2.20)	14.30	0.133
<i>L</i> (3.40)	25.60	0.236
<i>AKARI</i> /9	53.00	2.440
<i>IRAS</i> /12	38.90	1.550
<i>AKARI</i> /18	21.50	0.029
<i>IRAS</i> /25	17.10	0.684
<i>IRAS</i> /60	3.94	0.315
<i>MIPS</i> /70	2.03	0.034
<i>PACS</i> /70	2.13	0.003
<i>AKARI</i> /90	1.49	0.114
<i>IRAS</i> /100	2.00	0.160
<i>PACS</i> /100	1.04	0.0023
<i>MIPS</i> /160	0.297	0.00936
<i>PACS</i> /160	0.335	0.00211
<i>SPIRE</i> /250	0.0781	0.01170
<i>SPIRE</i> /350	0.0340	0.00510
<i>SPIRE</i> /500	0.0125	0.00434

**Table 4**  
RY Sgr Photometry

Band	Flux (Jy)	$\sigma$ (Jy)
<i>U</i> (0.365)	4.31	0.040
<i>B</i> (0.433)	9.77	0.090
<i>V</i> (0.550)	13.3	0.122
<i>R<sub>C</sub></i> (0.640)	14.30	0.132
<i>I<sub>C</sub></i> (0.790)	14.10	0.130
<i>J</i> (1.25)	13.5	0.124
<i>H</i> (1.60)	15.2	0.140
<i>K</i> (2.20)	23.8	0.219
<i>L</i> (3.40)	54.0	0.497
<i>WISE/3.4</i>	18.9	2.72
<i>WISE/4.6</i>	46.2	8.20
<i>AKARI/9</i>	48.0	3.66
<i>IRAS/12</i>	77.2	5.40
<i>WISE/12</i>	36.2	0.966
<i>AKARI/18</i>	20.2	1.02
<i>WISE/22</i>	14.0	0.232
<i>IRAS/25</i>	26.2	1.048
<i>IRAS/60</i>	5.43	0.489
<i>AKARI/65</i>	3.50	0.104
<i>MIPS/70</i>	2.92	0.021
<i>PACS/70</i>	4.39	0.008
<i>AKARI/90</i>	2.61	0.139
<i>IRAS/100</i>	4.60	0.414
<i>PACS/100</i>	3.31	0.007
<i>AKARI/140</i>	2.08	3 $\sigma$ upper limit
<i>MIPS/160</i>	1.34	0.030
<i>AKARI/160</i>	2.60	3 $\sigma$ upper limit
<i>PACS/160</i>	1.79	0.005
<i>SPIRE/250</i>	0.766	0.010
<i>SPIRE/350</i>	0.324	0.007
<i>SPIRE/500</i>	0.126	0.006

**Table 5**  
SU Tau Photometry

Band	Flux (Jy)	$\sigma$ (Jy)
<i>B</i> (0.433)	0.241	0.004
<i>V</i> (0.550)	0.560	0.010
<i>R<sub>C</sub></i> (0.640)	0.827	0.015
<i>I<sub>C</sub></i> (0.790)	0.977	0.018
<i>J</i> (1.25)	1.60	0.044
<i>H</i> (1.60)	1.70	0.047
<i>K</i> (2.20)	1.94	0.054
<i>L</i> (3.40)	3.57	0.099
<i>WISE/3.4</i>	3.62	0.260
<i>WISE/4.6</i>	11.1	0.675
<i>AKARI/9</i>	14.7	0.050
<i>IRAS/12</i>	9.48	0.759
<i>WISE/12</i>	7.77	0.079
<i>AKARI/18</i>	6.16	0.046
<i>WISE/22</i>	3.38	0.037
<i>MIPS/24</i>	3.07	0.037
<i>IRAS/25</i>	4.12	0.288
<i>IRAS/60</i>	1.54	0.139
<i>AKARI/65</i>	0.351	3 $\sigma$ upper limit
<i>MIPS/70</i>	0.322	0.003
<i>PACS/70</i>	0.523	0.002
<i>AKARI/90</i>	1.18	0.080
<i>IRAS/100</i>	2.87	0.315
<i>PACS/100</i>	0.318	0.002
<i>MIPS/160</i>	0.142	0.007
<i>PACS/160</i>	0.133	0.001
<i>SPIRE/250</i>	0.117	3 $\sigma$ upper limit
<i>SPIRE/350</i>	0.064	3 $\sigma$ upper limit
<i>SPIRE/500</i>	0.028	3 $\sigma$ upper limit

processing through a message passage interface (MPI). MOCASSIN was compiled with Intel’s “ifort” compiler, because it decreases the run time per model over free compilers such as gfortran. We used Open MPI for the MPI implementation. MOCASSIN is run by first defining a series of user inputs, such as number of dimensions, grid size, dust density, composition, and distribution. Interactions, whether absorption or scattering, between photons and dust grains are governed by Mie scattering theory (Ercolano et al. 2005). MOCASSIN returns the temperature, mass, and opacity of the dust shells.

For the sample, we chose to model these systems as a central point source surrounded by a gas-free dust shell. These shells are further assumed to be “smooth,” which means that there are no inhomogeneities (“clumps”), with the dust density profile falling by  $r^{-2}$  from the inner radius ( $R_{\text{in}}$ ) to the outer radius ( $R_{\text{out}}$ ). We further took advantage of axial symmetry to model only one-eighth of the envelope rather than a full envelope. The composition of the dust grains was determined by prior analysis of the spectra of RCB stars, which is consistent with amorphous Carbon (amC) grains (Hecht et al. 1984; Clayton et al. 2011b; García-Hernández et al. 2011b, 2013). This is due to the extinction curve peaking between 2400 and 2500 Å (Hecht et al. 1984) and the featureless nature of the spectra in the optical and IR (García-Hernández et al. 2011b). Thus, our MCRT models were performed with 100% amC grains. The grain size distribution was motivated by the findings of Hecht et al. (1984), who used *IUE* observations of R CrB and RY Sgr

to find that dust grain sizes appeared consistent with a distribution between 5 and 60 nm (0.005–0.06  $\mu\text{m}$ ). A power-law distribution following Mathis et al. (1977),  $a^{-3.5}$ , specifies the size distribution of the dust grains. Detailed discussion of the modeling of individual stars can be found in the next section.

#### 4.2. Semianalytic Modeling

We also modeled a subset of our SEDs (see Section 5.8.2) with a semianalytic Fortran code called QuickSAND (Quick Semi-Analytic Dust; Sugerman et al. 2012). The code computes an SED for a source surrounded by a spherical shell after being given the  $R_{\text{in}}$ ,  $R_{\text{out}}$ , source luminosity, source temperature, density profile for the shell, number density at  $R_{\text{in}}$ , dust composition, and distance to the object. The modeling is performed over a spherical polar grid. QuickSAND can be run to either generate a single SED or output a grid of SEDs over a predefined parameter space. We were provided a custom version that operates on an exponential grid to maximize resolution for shells that cover many orders of magnitude in size between  $R_{\text{in}}$  and  $R_{\text{out}}$ .

### 5. Circumstellar Shells of R Coronae Borealis Stars

A twofold approach was adopted for our investigation into the cold CSM of our sample RCB stars. First, the unpublished, archival *Spitzer* and *Herschel* images were examined by eye to identify morphological features. Next, the results from aperture

**Table 6**  
UW Cen Photometry

Band	Flux (Jy)	$\sigma$ (Jy)
<i>U</i> (0.365)	0.234	0.002
<i>B</i> (0.433)	0.594	0.005
<i>V</i> (0.550)	1.020	0.009
<i>R<sub>C</sub></i> (0.640)	1.170	0.011
<i>I<sub>C</sub></i> (0.790)	1.340	0.012
<i>J</i> (1.25)	1.350	0.025
<i>H</i> (1.60)	1.090	0.020
<i>K</i> (2.20)	0.879	0.016
<i>L</i> (3.40)	1.070	0.049
<i>WISE/3.4</i>	2.150	0.105
<i>IRAC/3.6</i>	5.260	0.026
<i>IRAC/4.5</i>	6.690	0.034
<i>WISE/4.6</i>	8.660	0.263
<i>IRAC/5.8</i>	7.690	0.054
<i>IRAC/8.0</i>	9.050	0.060
<i>AKARI/9</i>	9.760	0.070
<i>IRAS/12</i>	7.850	0.471
<i>WISE/12</i>	6.820	0.044
<i>AKARI/18</i>	5.700	0.047
<i>WISE/22</i>	4.570	0.046
<i>MIPS/24</i>	4.350	0.011
<i>IRAS/25</i>	5.750	0.345
<i>IRAS/60</i>	9.220	0.737
<i>AKARI/65</i>	6.650	0.413
<i>MIPS/70</i>	5.570	0.007
<i>PACS/70</i>	2.130	0.003
<i>AKARI/90</i>	7.300	0.332
<i>IRAS/100</i>	5.940	0.594
<i>PACS/100</i>	4.950	0.006
<i>AKARI/140</i>	4.180	0.349
<i>MIPS/160</i>	2.530	0.055
<i>AKARI/160</i>	2.810	1.020
<i>PACS/160</i>	2.470	0.004

or PSF photometry were used to fill in the FIR/submillimeter regime for the maximum-light SEDs of these stars. The goal of these two methods is to achieve a better understanding of the CSM of RCB stars. This, by extension, allows for a more accurate picture of the mass-loss history for these stars and a clearer idea of their progenitors.

As seen in the AAVSO light curves (Figures 1–4), we have made efforts to select to make sure that NIR observations and shorter were observed during maximum light. RCB stars are known to exhibit regular to semiregular pulsations,  $\Delta V \lesssim 0.1$  mag, and periods of 40–100 days (Lawson et al. 1990; Saio 2008). This effect has minimal impact on our SED modeling. However, the *IUE* observations, despite being dereddened using CCM, are sensitive to small amounts of dust.

### 5.1. *MV Sgr*

Variability in *MV Sgr* was first discovered by Woods (1928). It would be another 30 years until it was identified as an RCB star (Hoffleit 1958, 1959). Hoffleit (1959) also discussed the results of early spectra reported by Herbig (1964), which confirmed the hydrogen deficiency of *MV Sgr*. However, what was unexpected was that the spectrum of *MV Sgr* revealed that it was similar in temperature to a B-type star.

**Table 7**  
V854 Cen Photometry

Band	Flux (Jy)	$\sigma$ (Jy)
<i>U</i> (0.365)	1.450	0.036
<i>B</i> (0.433)	3.820	0.095
<i>V</i> (0.550)	5.500	0.137
<i>R<sub>C</sub></i> (0.640)	6.067	0.152
<i>I<sub>C</sub></i> (0.790)	6.512	0.163
2MASS/ <i>J</i> (1.24)	5.756	0.095
<i>J</i> (1.25)	6.998	0.193
<i>H</i> (1.60)	8.268	0.229
2MASS/ <i>H</i> (1.66)	5.399	0.085
2MASS/ <i>K<sub>S</sub></i> (2.16)	7.480	0.124
<i>K</i> (2.20)	12.50	0.345
<i>L</i> (3.40)	27.50	0.761
<i>AKARI/9</i>	23.00	1.170
<i>IRAS/12</i>	23.00	1.150
<i>AKARI/18</i>	7.364	0.033
<i>MIPS/24</i>	4.944	0.001
<i>IRAS/25</i>	7.820	0.469
<i>IRAS/60</i>	1.510	0.136
<i>AKARI/65</i>	0.940	3 $\sigma$ upper limit
<i>MIPS/70</i>	0.641	0.001
<i>PACS/70</i>	2.132	0.003
<i>AKARI/90</i>	0.705	0.036
<i>IRAS/100</i>	1.030	3 $\sigma$ upper limit
<i>AKARI/140</i>	0.185	3 $\sigma$ upper limit
<i>MIPS/160</i>	0.068	0.001
<i>AKARI/160</i>	1.040	3 $\sigma$ upper limit

**Table 8**  
V CrA Photometry

Band	Flux (Jy)	$\sigma$ (Jy)
<i>U</i> (0.365)	0.138	0.003
<i>B</i> (0.433)	0.364	0.007
<i>V</i> (0.550)	0.444	0.008
<i>J</i> (1.25)	0.681	0.019
<i>H</i> (1.60)	0.804	0.022
<i>K</i> (2.20)	1.180	0.033
<i>L</i> (3.40)	3.080	0.085
<i>WISE/3.4</i>	1.400	0.139
<i>WISE/4.6</i>	3.490	0.286
<i>AKARI/9</i>	3.610	0.210
<i>IRAS/12</i>	5.660	0.226
<i>WISE/12</i>	3.820	0.053
<i>AKARI/18</i>	2.170	0.013
<i>WISE/22</i>	1.960	0.025
<i>MIPS/24</i>	1.520	0.003
<i>IRAS/25</i>	2.460	0.172
<i>IRAS/60</i>	0.405	0.036
<i>MIPS/70</i>	0.272	0.004
<i>PACS/70</i>	0.263	0.003
<i>AKARI/90</i>	1.490	0.114
<i>IRAS/100</i>	1.320	3 $\sigma$ upper limit
<i>PACS/100</i>	0.135	0.003
<i>MIPS/160</i>	0.117	3 $\sigma$ upper limit
<i>PACS/160</i>	0.051	0.005
<i>SPIRE/250</i>	0.050	3 $\sigma$ upper limit
<i>SPIRE/350</i>	0.013	3 $\sigma$ upper limit
<i>SPIRE/500</i>	0.006	3 $\sigma$ upper limit

**Table 9**  
V605 Aql Photometry

Band	Flux (Jy)	$\sigma$ (Jy)
<i>J</i> (1.25)	3.21e-05	1.50e-05
<i>H</i> (1.60)	2.27e-04	3.00e-05
<i>K</i> (2.20)	8.56e-04	8.00e-05
<i>WISE</i> /3.4	1.44e-02	3.05e-04
<i>WISE</i> /4.6	1.13e-01	2.07e-03
<i>AKARI</i> /9	2.85e+00	1.68e-02
<i>IRAS</i> /12	4.99e+00	2.00e-01
<i>WISE</i> /12	8.56e+00	5.52e-02
<i>AKARI</i> /18	1.53e+01	1.20e-01
<i>WISE</i> /22	2.22e+01	1.02e-01
<i>MIPS</i> /24	1.57e+01	8.01e-02
<i>IRAS</i> /25	2.95e+01	1.18e+00
<i>IRAS</i> /60	4.07e+01	4.10e+00
<i>AKARI</i> /65	2.67e+01	2.50e+00
<i>MIPS</i> /70	1.78e+01	1.85e-01
<i>AKARI</i> /90	2.08e+01	9.87e-01
<i>IRAS</i> /100	1.83e+01	2.00e+00
<i>MIPS</i> /160	2.82e+00	1.12e-01

**Table 10**  
HD 173409 Photometry

Band	Flux (Jy)	$\sigma$ (Jy)
<i>U</i> (0.365)	0.095	0.002
<i>B</i> (0.433)	0.324	0.006
<i>V</i> (0.550)	0.626	0.012
<i>R<sub>C</sub></i> (0.640)	0.733	0.014
<i>I<sub>C</sub></i> (0.790)	0.770	0.014
2MASS/ <i>J</i> (1.24)	0.698	0.017
<i>J</i> (1.25)	0.739	0.020
<i>H</i> (1.60)	0.531	0.015
2MASS/ <i>H</i> (1.66)	0.475	0.020
2MASS/ <i>K<sub>S</sub></i> (2.16)	0.354	0.012
<i>K</i> (2.20)	0.356	0.010
<i>L</i> (3.40)	0.190	0.009
<i>WISE</i> /3.4	0.185	0.004
<i>WISE</i> /4.6	0.102	0.002
<i>WISE</i> /12	0.020	0.0004
<i>WISE</i> /25	0.004	0.001
PACS/70	7.06e-05	3 $\sigma$ upper limit
PACS/100	1.47e-04	3 $\sigma$ upper limit
PACS/160	1.48e-04	3 $\sigma$ upper limit
SPIRE/250	0.113	3 $\sigma$ upper limit
SPIRE/350	0.001	3 $\sigma$ upper limit
SPIRE/500	0.002	3 $\sigma$ upper limit

This extreme temperature makes this star a member of the unique subset of “hot” RCB stars (of which only four are known; De Marco et al. 2002). Pandey et al. (1996) found the Li I 6708 Å line in emission.

### 5.1.1. Image Inspection

MV Sgr was not observed with *Herschel*, so the *Spitzer*/*MIPS* observations are the only FIR images of this star. Postage stamp images from *MIPS* can be seen in Figure 5. MV Sgr appears as a point source at 24  $\mu\text{m}$ , as the warm dust remains unresolved. The emission at 70  $\mu\text{m}$  measures colder dust,

farther from the central star, but this dust is also unresolved. No emission is detected in the *MIPS* 160  $\mu\text{m}$  observation.

### 5.1.2. Radiative Transfer Modeling

Archival photometry and spectroscopy were combined with new photometry from the *Spitzer*/*MIPS* observations to construct the SED for MV Sgr. See Table 2 for the input values. The maximum-light SED is presented in Figure 6 along with the best-fit MOCASSIN models. The SED in the UV/optical is fit well by a  $T_{\text{eff}} = 16,000$  K blackbody as determined by Drilling et al. (1984) and De Marco et al. (2002). The input luminosity for the MOCASSIN modeling was determined by assuming an absolute magnitude  $M_V = -3.0$  for the hot RCB stars (Tisserand et al. 2009). This corresponds to a distance of 11.5 kpc and luminosity of  $\sim 5200 L_{\odot}$ .

The effect of a strong IR excess can be seen after 1.0  $\mu\text{m}$  as the SED continues to rise as wavelength increases. The IR component was best fit by two concentric, smooth shells with density falling as  $r^{-2}$ . This modeling strategy is reinforced with a “by eye” examination of the SED where the presence of two separate components in the IR can be easily seen. The first peak is at  $\sim 4.6$   $\mu\text{m}$  and corresponds to an envelope beginning at  $3.45 \times 10^{14}$  cm and extending to  $9.45 \times 10^{15}$  cm. The dust mass is  $7.59 \times 10^{-8} M_{\odot}$ , while temperatures range from 1000 K down to 200 K at the inner and outer radii, respectively. The second peak occurs at  $\sim 25$   $\mu\text{m}$  with a best-fit envelope having an inner radius  $3.25 \times 10^{16}$  cm and outer radius  $9.45 \times 10^{17}$  cm. Dust temperatures in the shell range from 150 to 50 K with a mass of  $3.27 \times 10^{-4} M_{\odot}$ .

The shape of the SED in the IR regime was also examined by García-Hernández et al. (2011b, 2013). García-Hernández et al. (2011b) found that the two blackbody curves have temperatures 1500 and  $\sim 200$  K, which agree with temperatures from our MCRT modeling. MV Sgr has been among the least active of RCB stars in terms of decline events. In all the years of monitoring this star, there have only been three observed declines (Hoffleit 1959; Landolt & Clem 2017). In spite of this seemingly low level of activity, the dust mass in the outer envelope is about the same as other RCB stars in our sample. This is due to the puff-like nature of dust formation events. Declines only happen when the cloud condenses along our line of sight with the RCB star. There can be any number of puffs, at any time, forming around the central RCB star that we are not able to detect in the visible (García-Hernández et al. 2011b, 2013; Rao & Lambert 2015). Thus, an appreciable envelope with a reservoir of cold dust can still be constructed even if a star is observed to remain at maximum light.

## 5.2. R CrB

R CrB is the eponymous member of the RCB class, having been first discovered as variable in the late 18th century (Pigott & Englefield 1797). Bidelman (1953) was among the first to note the hydrogen-deficient but carbon-rich nature of R CrB and RCB stars. Keenan & Greenstein (1963) first identified the star as having Li via the 6708 Å feature. R CrB has also been found to be enriched with  $^{19}\text{F}$  via lines at 6902.47 and 6834.26 Å (Pandey et al. 2008).

### 5.2.1. Image Inspection

Observations of R CrB in the FIR and submillimeter were previously inspected and discussed by Clayton et al. (2011a),



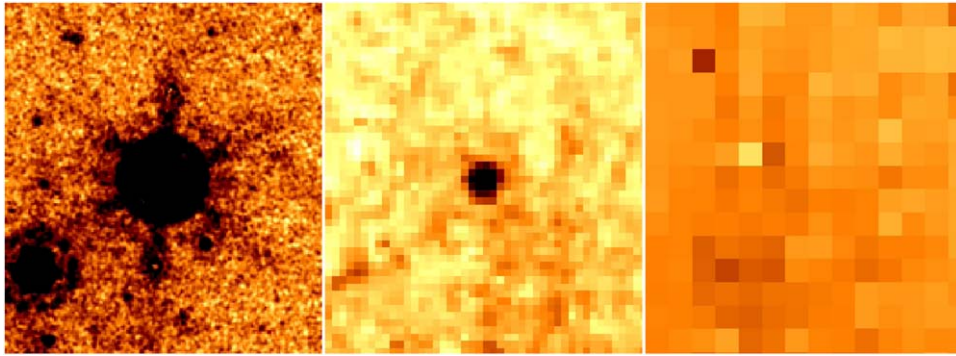


**Figure 5.** *Spitzer*/MIPS view of MV Sgr. The panels are (left to right) 24, 70, and 160  $\mu\text{m}$ , respectively, and the field of view is  $3\frac{1}{6} \times 4\frac{1}{0}$ . North is up and east is left.

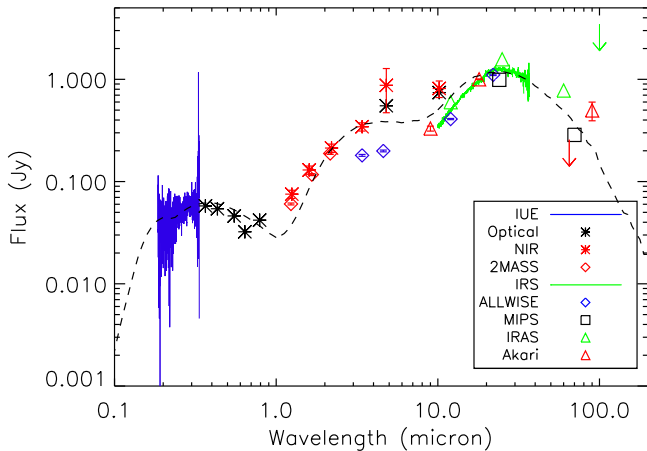


**Figure 6.** Maximum-light SED of MV Sgr. Blue line: *IUE* spectrum; black asterisks: *UBVR<sub>c</sub>ICMN*; red asterisks: *JHKLMN*; open red diamonds: 2MASS *JHK<sub>s</sub>*; open blue diamonds: *WISE* (3.4, 4.6, 12.0, 22.0  $\mu\text{m}$ ); green line: *Spitzer*/IRS spectrum; open black squares: *Spitzer*/MIPS (24 and 70  $\mu\text{m}$ ); open green triangles and arrow ( $3\sigma$ ): *IRAS* (12, 25, 60, 100  $\mu\text{m}$ ); open red triangle and arrow ( $3\sigma$ ): *AKARI* (60 and 100  $\mu\text{m}$ ). The sum of the best-fit MOCASSIN models for the central source, warm, and cold dust shells is represented by the dashed black line.

which included both *Spitzer*/MIPS and *Herschel*/SPIRE. *Herschel*/PACS observations were taken after the paper was published and are presented here for the first time. Figure 7 contains the complete nine-panel postage stamp series of the MIPS, PACS, and SPIRE images of R CrB.

Previous discussions of R CrB’s nebosity point to the spherical nature of its morphology (Gillett et al. 1986; Clayton et al. 2011a). These works had at their disposal the highest sensitivity and angular resolution FIR/submillimeter observations for their time. The *Herschel*/PACS images reinforce the apparent spherical shape of the R CrB nebosity.

### 5.2.2. Radiative Transfer Modeling

The maximum-light SED of R CrB was originally modeled and presented by Clayton et al. (2011a). New photometry from the *Herschel*/PACS observations of R CrB was added to the Clayton et al. (2011a) SED and remodeled using MOCASSIN. The SED is displayed in Figure 8 with the input photometry held in Table 3. The best-fit MOCASSIN model is represented by the dashed line. Parameters from Clayton et al. (2011a) were adopted for our own MCRT modeling. These include an effective temperature of 6750 K and distance of 1.40 kpc, which result in a luminosity of  $9150 L_{\odot}$ .

The R CrB SED was best modeled using two concentric dust envelopes. The inner shell extends from  $1.00 \times 10^{15}$  cm to  $3.00 \times 10^{16}$  cm. The mass of this envelope was found to be  $9.09 \times 10^{-7} M_{\odot}$  with dust temperatures ranging from 700 K down to 180 K. A second envelope was modeled to account for the presence of additional colder material that one envelope cannot entirely account for. This outer shell has an inner radius of  $3.40 \times 10^{17}$  cm and outer radius of  $1.00 \times 10^{19}$  cm. The dust mass contained in this envelope is  $2.42 \times 10^{-4} M_{\odot}$  with temperatures ranging from 80 to 20 K.

R CrB is, by far, the best studied of any RCB star, so it comes as no surprise that its SED has also been extensively studied (Gillett et al. 1986; Rao & Nandy 1986; Goldsmith et al. 1990; Young et al. 1993a, 1993b; Nagendra & Leung 1996; Walker et al. 1996; Lambert et al. 2001; Clayton et al. 2011a; García-Hernández et al. 2011b; Rao & Lambert 2015).

We have compared our MOCASSIN results to those of García-Hernández et al. (2011b) and Clayton et al. (2011a). Rao & Lambert (2015) build on the work presented by García-Hernández et al. (2011b) and focus more on tracking changes in the brightnesses of RCB stars in the 30 years of space-based MIR observations. A two-component (star + single IR excess) blackbody fit was used by García-Hernández et al. (2011b) to describe the R CrB SED. They described the stellar component with a blackbody of  $T_{\text{star}} = 6750$  K (derived from Asplund et al. 2000) and the IR excess with a blackbody that had a maximum dust temperature of 950 K, which was based on the *Spitzer*/IRS spectrum between 10 and 20  $\mu\text{m}$  (García-Hernández et al. 2011b).

Clayton et al. (2011a) presented the results of their full 3D (spherical polar grid) MCRT code. The code included nonisotropic scattering, polarization, and thermal emission from dust (Whitney et al. 2003b, 2003a; Robitaille et al. 2006). The best-fit model found that the observed SED could be explained by the presence of a dusty disk surrounded by a larger envelope. The disk extended from  $6.28 \times 10^{14}$  cm to  $2.24 \times 10^{15}$  cm and had a dust mass of  $3.5 \times 10^{-6} M_{\odot}$  (Clayton et al. 2011a). The shell had radii of  $1.95 \times 10^{18}$  cm and  $1.32 \times 10^{19}$  cm at the inner and outer boundaries, respectively (Clayton et al. 2011a). The dust mass of the Clayton et al. envelope was also found to be roughly two orders of magnitude higher ( $\sim 2.0 \times 10^{-2} M_{\odot}$ ). This discrepancy is attributed to Clayton et al. using a luminosity of  $5645 L_{\odot}$ , which is roughly a factor of two lower than our input luminosity, and a full MRN size distribution (Mathis et al. 1977).

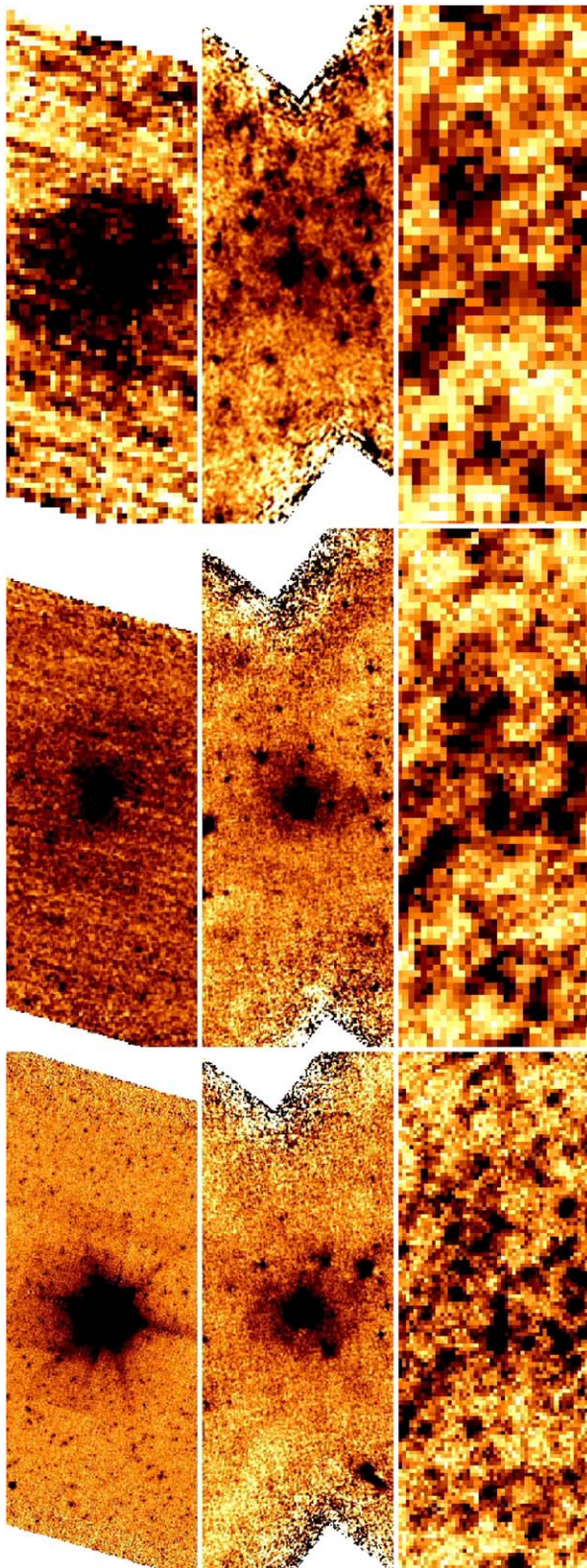


**Figure 7.** First row (beginning lower left corner): *Spitzer*/MIPS observations of R CrB 24, 70, 160  $\mu\text{m}$ , respectively. The field of view shown for all three bands is  $25' \times 10'$ . Second row: *Herschel*/PACS observations of R CrB at 70, 100, and 160  $\mu\text{m}$ , respectively. The field of view shown for all three bands is  $12' \times 5'$ . Third row: *Herschel*/SPIRE observations of R CrB at 250, 350, and 500  $\mu\text{m}$ , respectively. The field of view shown for all three bands is  $13'5 \times 5'0$ . North is left and east is down.

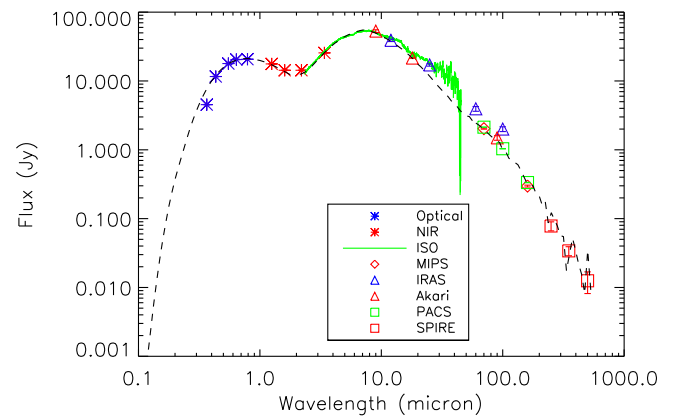


**Figure 8.** Maximum-light SED of R CrB. Blue asterisks: *UBVR<sub>C</sub>I<sub>C</sub>*; red asterisks: *JHKL*; green line: *ISO* spectrum; open red triangles: *AKARI* (9, 18, 90  $\mu\text{m}$ ); open red diamonds: *Spitzer*/MIPS (24 and 70  $\mu\text{m}$ ); open blue triangles: *IRAS* (12, 25, 60, 100  $\mu\text{m}$ ); open green squares: *Herschel*/PACS (70, 100, 160  $\mu\text{m}$ ); open red squares: *Herschel*/SPIRE (250, 350, 500  $\mu\text{m}$ ). The sum of the best-fit MOCASSIN models for the central source, warm, and cold dust shells is represented by the dashed black line.

### 5.3. RY Sgr

RY Sgr was first suspected to be variable in 1893 while under observation by Colonel E. E. Markwick while he was stationed in Gibraltar (Pickering 1896; Shears 2011). Pickering (1896) also noted that the spectrum of the new variable was found to be peculiar after being discovered by Williamina Fleming. By the early 1950s, RY Sgr was known to be hydrogen-deficient and classified as an RCB star (Bidelman 1953). Lambert & Rao (1994) found no evidence for Li overabundance in the spectrum of RY Sgr. The presence of  $^{19}\text{F}$  was found in RY Sgr's atmosphere from absorption lines located at 6902 and 6834  $\text{\AA}$  (Pandey et al. 2008). RCB stars, as a class, are known to show brightness fluctuations via pulsations in addition to their spectacular declines. RY Sgr was first discovered to be pulsating with 0.5 mag variations and a period of  $\sim 39$  days by Campbell & Jacchia (1941).

#### 5.3.1. Image Inspection

Diffuse nebulosity surrounding RY Sgr was searched for in the unpublished, archival *Spitzer*/MIPS, *Herschel*/PACS, and *Herschel*/SPIRE observations. These observations provide the highest angular resolution and sensitivity for RY Sgr from 24 to 500  $\mu\text{m}$ . A nine-panel mosaic containing these images is found in Figure 9.

RY Sgr appears as a point source in the *Spitzer*/MIPS 24  $\mu\text{m}$  image. RY Sgr begins to become more extended in the 70 and 160  $\mu\text{m}$  observations, but the angular resolution at MIPS is not high enough to separate out the PSF from any diffuse nebulosity. *Herschel*/PACS was able to provide the necessary angular resolution to resolve the diffuse nebulosity surrounding RY Sgr. The diffuse structure appears spherical. Yet, the density of the shell appears to be higher in the northern region than in the southern. This is reinforced with the *Herschel*/SPIRE observations at 250 and 350  $\mu\text{m}$ , where the angular resolution and sensitivity are still high enough to resolve the shell from the background. However, by 500  $\mu\text{m}$ , the emission from the envelope has become too weak to resolve

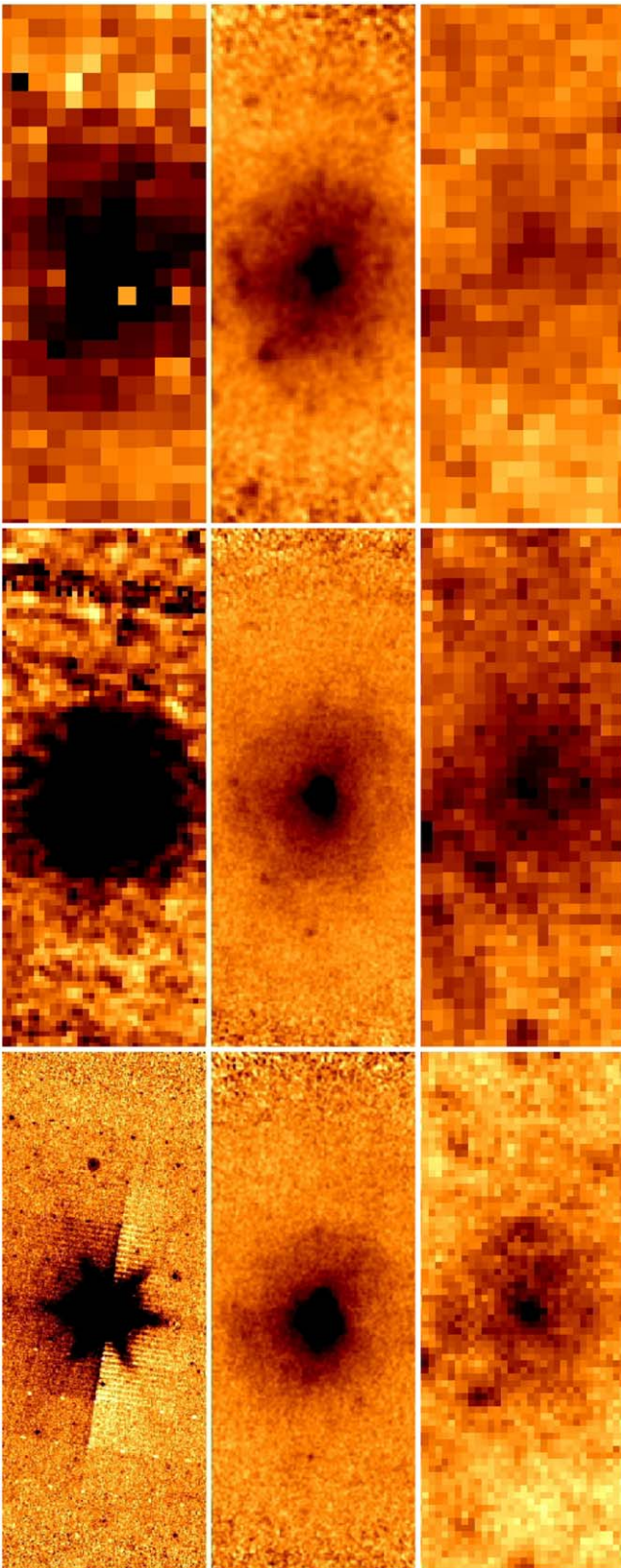


**Figure 9.** First row (beginning lower left corner): *Spitzer*/MIPS observations of RY Sgr 24, 70, 160  $\mu\text{m}$ , respectively. Second row: *Herschel*/PACS observations of RY Sgr at 70, 100, and 160  $\mu\text{m}$ , respectively. Third row: *Herschel*/SPIRE observations of RY Sgr at 250, 350, and 500  $\mu\text{m}$ , respectively. The field of view in the *Spitzer*/MIPS 24  $\mu\text{m}$  is  $15'.5 \times 6'.1$ , while the remaining panels are all  $7'.6 \times 3'.2$ . North is left and east is down.

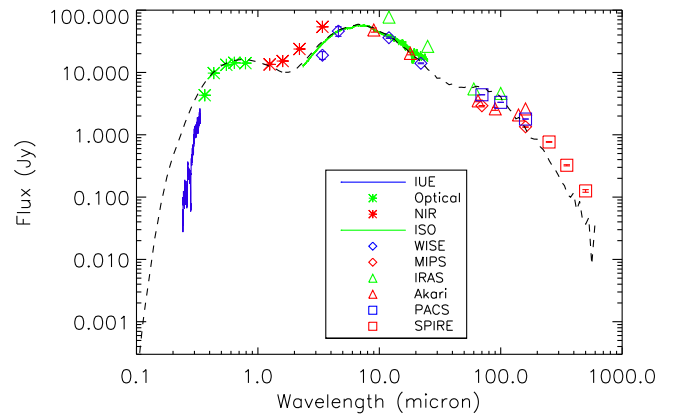


**Figure 10.** Maximum-light SED of RY Sgr. Blue line: *IUE* spectrum; green asterisks:  $UBVR_C I_C$ ; red asterisks: *JHKL*; green line: *ISO* spectrum; open blue diamonds: *WISE* (3.4, 4.6, 12.0, 22.0  $\mu\text{m}$ ); open red triangles: *AKARI* (9, 18, 90, 140, 160  $\mu\text{m}$ ); open red diamonds: *Spitzer*/MIPS (70 and 160  $\mu\text{m}$ ); open green triangles: *IRAS* (12, 25, 60, 100  $\mu\text{m}$ ); open blue squares: *Herschel*/PACS (70, 100, 160  $\mu\text{m}$ ); open red squares: *Herschel*/SPIRE (250, 350, 500  $\mu\text{m}$ ). The sum of the best-fit MOCASSIN models for the central source, warm, and cold dust shells is represented by the dashed black line.

anything more than a rough determination of the location of the nebulosity.

### 5.3.2. Radiative Transfer Modeling

The available photometry and spectroscopy for RY Sgr (while at maximum light) were combined to construct its SED, which can be seen in Figure 10. The dashed line represents the best-fit MCRT model from MOCASSIN. The photometry is found in Table 4. A blackbody with  $T_{\text{eff}} = 7250$  K was adopted from atmosphere modeling by Asplund et al. (2000). A distance of 1.5 kpc was determined by assuming an absolute *V*-band magnitude of  $-5$  (Tisserand et al. 2009). This results in an input luminosity of  $8900 L_{\odot}$  for RY Sgr.

The SED begins to be dominated by the RY Sgr CSM after 1.6  $\mu\text{m}$  (*H* band) due to contributions from warm dust close to the central star. A spherical envelope with inner radius at  $8.62 \times 10^{14}$  cm and outer radius at  $5.00 \times 10^{16}$  cm describes the SED between 1.6 and  $\sim 25.0$   $\mu\text{m}$ . The dust mass of this envelope is  $8.90 \times 10^{-7} M_{\odot}$  with temperatures ranging from  $\sim 500$  K down to  $\sim 200$  K. This wavelength region of the RY Sgr SED was also examined by García-Hernández et al. (2011b). The central star was represented by a blackbody of 7200 K. The maximum temperature of the blackbody used to fit this dust component was found to be 675 K (García-Hernández et al. 2011b).

However, a second blackbody peak can clearly be seen in the photometry longer than 40  $\mu\text{m}$  that does not lie on the Rayleigh–Jeans tail of the first IR excess. A second envelope was modeled with an inner radius at  $5.15 \times 10^{17}$  cm and extending outward to  $4.50 \times 10^{18}$  cm. The dust mass of this envelope is  $7.25 \times 10^{-4} M_{\odot}$  with temperatures ranging from  $\sim 60$  K down to  $\sim 30$  K.

### 5.4. SU Tau

Variability in SU Tau was first noted by Cannon & Pickering (1908) with a note that it could be an RCB star. This classification was strengthened further in a later *Harvard*

*College Observatory Bulletin* (Barnard 1916). SU Tau, like R CrB, has been found to be rich in Li and  $^{19}\text{F}$  (Lambert & Rao 1994; Pandey et al. 2008).

#### 5.4.1. Image Inspection

Unpublished FIR and submillimeter observations of SU Tau exist from *Spitzer*/MIPS, *Herschel*/PACS, and *Herschel*/SPIRE. These observations are presented as a nine-panel postage stamp image in Figure 11. The sensitivity with *Spitzer*/MIPS is enough to detect the presence of dust surrounding SU Tau, but the angular resolution is not sufficient to separate nebulosity from the PSF.

The need for improved angular resolution becomes quickly apparent when examining the *Herschel* observations. The galaxy, 2MFGC 4715 (Mitronova et al. 2004), and the SU Tau CSM, which are blended in the *Spitzer*/MIPS  $70\ \mu\text{m}$  image, are well separated and can also be further distinguished in three-color images, which can be found in Figure 12. The morphology of SU Tau's CSM is unlike that found around any other RCB star. A bow-shock-type feature, which dominates the eastern half of the image, is clearly visible in observations with both *Herschel* instruments with definitive detections out to  $350\ \mu\text{m}$ . Diffuse nebulosity can be discerned in the western half of the PACS three-color image.

The outer edge of the bow shock extends  $\sim 30''$ – $50''$  from the central position of SU Tau (see Figure 13). This corresponds to a physical distance of 7.4–10.8 pc assuming the distance to SU Tau is 3.3 kpc (see below). The flux of the large overdensity, located in the southeast, was sampled in the *Herschel*/PACS observations with an elliptical region with semimajor axis of  $2''.9$  and semiminor axis of  $1''.8$ . The measured fluxes were 0.0284, 0.0328, and 0.0193 Jy at 70, 100, and  $160\ \mu\text{m}$ , respectively. These values correspond to 5%, 10%, and 15% of the calculated flux for the dust emission centered on SU Tau (see below). Estimated dust temperatures located at the outer edge of the bow shock are about 30 K. This is consistent with a blackbody with a peak wavelength of  $100\ \mu\text{m}$ , which is exactly where the maximum flux value for the overdensity was found to be.

It is difficult to determine for certain how long any interaction between the SU Tau CSM and the ISM has been occurring. If we assume that any interaction is much less than the time for the material to expand outward to its current distance from the central star, then we can at least put some bound on its age. If this material is part of a fossil PN structure, as predicted in the FF scenario, then it would take the material between  $2.4 \times 10^5$  and  $5.3 \times 10^5$  years to reach its current location. This assumes that the initial shell was expanding at typical PNe velocities ( $20$ – $30\ \text{km s}^{-1}$ ). However, in the DD scenario, the dust would have outward velocities of at least  $400$ – $900\ \text{km s}^{-1}$ . The lower limit comes from observations of the He I  $\lambda 10830$  line (Clayton et al. 1992a, 2003, 2013a), while the upper limit comes from simulations of WD mergers (Montiel et al. 2015). These velocities indicate the dust would reach the determined distances on the order of  $10^4$  years.

A search for evidence of this feature in archival observations of SU Tau found what could be diffuse emission associated with the bow shock in the 2MASS *J* band (see Figure 14). The 2MASS *J*-band filter has a central wavelength of  $1.235 \pm 0.006\ \mu\text{m}$  with a bandwidth of  $0.162 \pm 0.001\ \mu\text{m}$  (Cohen et al. 2003). The

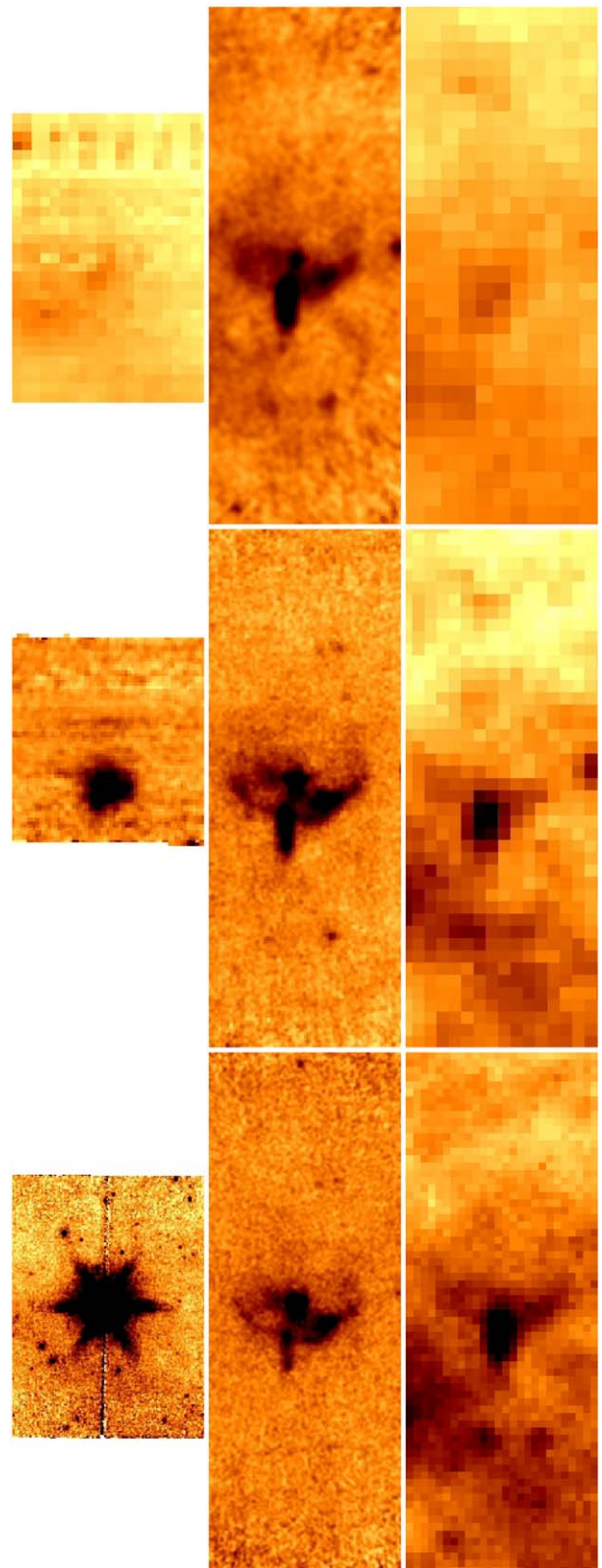


**Figure 11.** First row (starting lower left corner): *Spitzer*/MIPS observations of SU Tau 24, 70,  $160\ \mu\text{m}$ , respectively. The fields of view of the observations (not including white space) are  $8'.5 \times 5'.75$ ,  $5'.45 \times 5'.0$ , and  $8'.4 \times 5'.25$ , respectively. Second row: *Herschel*/PACS observations of SU Tau at 70, 100, and  $160\ \mu\text{m}$ , respectively. Third row: *Herschel*/SPIRE observations of SU Tau at 250, 350, and  $500\ \mu\text{m}$ , respectively. The fields of view of the *Herschel* observations are all  $7' \times 2'.5$ . North is left and east is down.

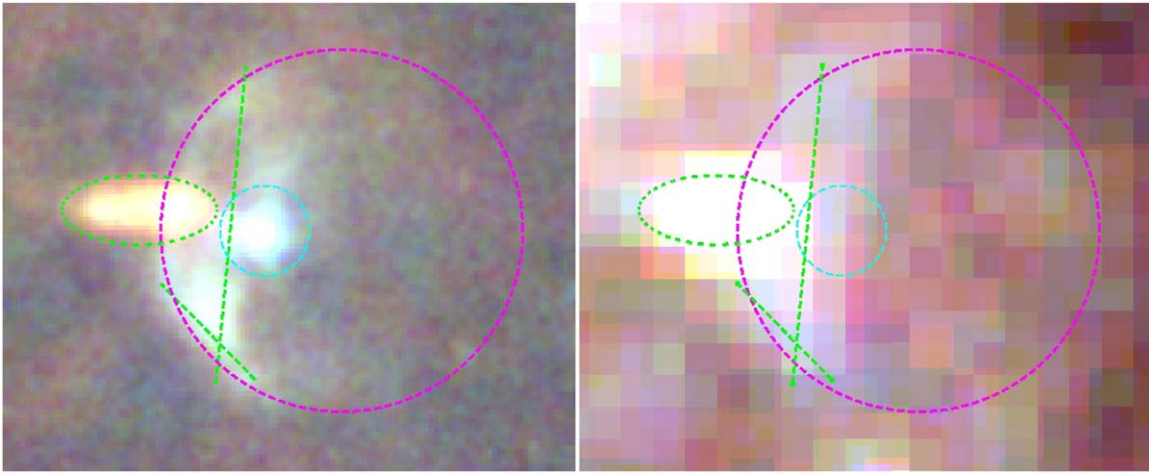


**Figure 12.** Left: three-color *Herschel*/PACS image with the 70, 100, and 160  $\mu\text{m}$  observations being represented by blue, green, and red, respectively. Right: three-color *Herschel*/SPIRE image with 250, 350, and 500  $\mu\text{m}$  observations being represented by blue, green, and red, respectively. The field of view in both frames is  $3' \times 2.4'$ . The cyan circle (radius =  $14''$ ) is centered on the position of SU Tau, the green ellipse shows the background galaxy separate from SU Tau, and the green lines ( $1'.66$  and  $0'.7$  in length) are there to guide the eye to the bow shock feature being associated with SU Tau. The magenta circle (radius =  $0'.95$ ) is centered to have a section of its arc pass through the bow shock and to highlight the diffuse emission west of SU Tau. These observations are now oriented in the traditional astronomical sense: north is up and east is left.

wavelength of the electron transition between the fifth and third energy levels of hydrogen (Paschen- $\beta$ ) is  $1.282 \mu\text{m}$ , which falls within the 2MASS  $J$ -band bandwidth.

Stellar bow shocks typically manifest from interactions between the stellar wind of a rapidly moving star and the denser, slower ISM through which the star is currently moving. Bow shocks have been detected in the FIR around other stars (e.g., R Hydrae, Ueta et al. 2006; Betelgeuse, Decin et al. 2012; Cox et al. 2012). The obvious difference between SU Tau, as well as other RCB stars, and these other stars is the extreme hydrogen deficiency that RCB stars are known to have. The bow shock seen around Betelgeuse is caused by material lost during the red supergiant phase (Decin et al. 2012) running into the denser ISM in the direction of the star's motion. In the case of SU Tau, this lends itself to the question, what is the composition of the material being shocked? If SU Tau was formed via the FF scenario, then having H-rich material at the outskirts of its CSM is not surprising. However, we are only seeing emission from dust in the bow shock and are not able to comment on the composition of any gas associated with the SU Tau bow shock.

#### 5.4.2. Radiative Transfer Modeling

SU Tau's archival maximum-light photometry and spectroscopy were combined with photometry from the unpublished *Spitzer*/MIPS, *Herschel*/PACS, and *Herschel*/SPIRE ( $3\sigma$  upper limits) observations to construct its SED, which can be seen in Figure 15. The bow shock feature was not included in the photometry aperture, and the background galaxy was masked out in all *Herschel* observations. Further, it is highly likely that the *IRAS* 60  $\mu\text{m}$ , 100  $\mu\text{m}$ , and *AKARI* 100  $\mu\text{m}$  points are contaminated by flux from the background galaxy. These points are still included on the SED but had no influence on determining the final fit model. The dashed line represents the best-fit MCRT model from MOCASSIN. The photometry is found in Table 5. A blackbody with  $T_{\text{eff}} = 6500 \text{ K}$  was adopted from atmosphere modeling by Asplund et al. (2000). A distance of 3.3 kpc was determined by assuming an absolute  $V$ -band magnitude of  $-5$  (Tisserand

et al. 2009). This results in an input luminosity of  $10,450 L_{\odot}$  for SU Tau.

The SU Tau CSM begins to dominate the SED beginning around 2.2  $\mu\text{m}$  ( $K$  band), which indicates the presence of warm dust. A spherical envelope with inner radius at  $2.10 \times 10^{15} \text{ cm}$  and outer radius at  $4.25 \times 10^{16} \text{ cm}$  describes the SED from 1.6  $\mu\text{m}$  out to barely before the 70.0  $\mu\text{m}$  points. The dust mass of this envelope is  $2.27 \times 10^{-6} M_{\odot}$  with temperatures ranging from  $\sim 600 \text{ K}$  down to  $\sim 150 \text{ K}$ . This regime was also included in the blackbody fitting analysis by García-Hernández et al. (2011b). They were able to fit a blackbody temperature of 6500 K, which agrees with the temperature determined by Asplund et al. (2000). The IR excess was fit with a 635 K blackbody (García-Hernández et al. 2011b), which is in agreement with the temperature range from our MOCASSIN RT modeling.

However, a second excess can be seen to arise for photometry longer than 70  $\mu\text{m}$  as the points lie above the single-dust-envelope model fits. A second envelope was added with an inner radius at  $1.00 \times 10^{18} \text{ cm}$  and extending outward to  $9.00 \times 10^{18} \text{ cm}$ . The dust mass of this envelope is  $6.80 \times 10^{-4} M_{\odot}$  with temperatures ranging from  $\sim 50 \text{ K}$  down to  $\sim 25 \text{ K}$ .

#### 5.5. UW Cen

Brightness fluctuations in UW Cen were first noticed by Leavitt & Pickering (1906) when it exhibited a 1.6 mag change. Gaposchkin (1952) first suggested that UW Cen is an RCB star. UW Cen is one of two stars (the other is V854 Cen; see below) that have been examined for  $^{18}\text{O}$ ,  $^{19}\text{F}$ , and Li. Lithium has been known in UW Cen since Lambert & Rao (1994) found the Li resonance doublet at 6707  $\text{\AA}$  in its spectrum. Pandey et al. (2008) discovered  $^{19}\text{F}$  by absorption lines at 6834.26, 6902.47, 7398.68, and 7425.6  $\text{\AA}$ . The search for  $^{18}\text{O}$  resulted in a null detection owing to UW Cen being too warm to display molecular features (García-Hernández et al. 2009).

The CSM of UW Cen is unique among all of the RCB stars. It is the only RCB star discovered to have a reflection nebula surrounding it (Pollacco et al. 1991; Clayton et al. 1999). The nebula is  $\sim 15''$  in diameter. It is only visible either during deep

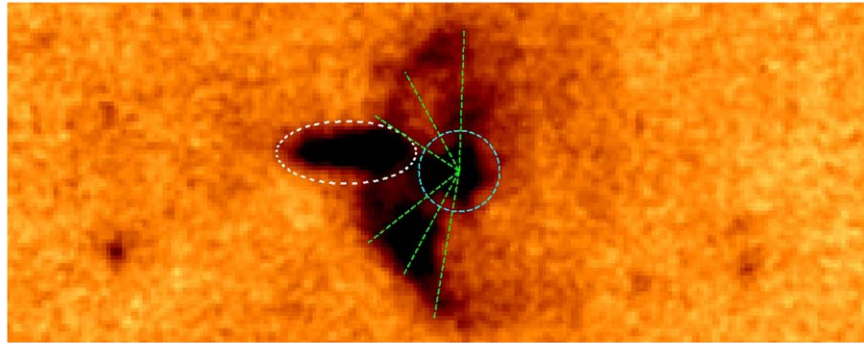


**Figure 13.** A zoom-in ( $5''.0 \times 2''.0$ ) of the *Herschel*/PACS  $100 \mu\text{m}$  observation of SU Tau. The white ellipse marks the background galaxy, 2MFGC 4715, while the cyan circle (radius =  $14''$ ) is centered on SU Tau. The six rays beginning from the central coordinates of SU Tau and extending out to the bow shock are about  $30''$ – $50''$  in length. North is up and east is left.

declines when the dust along the line of sight serves as a “natural” coronagraph or when an actual coronagraph is used to block the light from the central star. Clayton et al. (1999) found that the morphology of the nebula had changed significantly from year to year. These changes were too fast for any physical changes in the nebula to be occurring. Clayton et al. (1999) deduced that the changing pattern of new dust clouds condensing around the star resulted in variations in how the reflection nebula was illuminated.

#### 5.5.1. Image Inspection

The longest-wavelength photometric observations of UW Cen that had been previously examined were the *IRAS* observations from the 1980s (Schaefer 1986; Walker 1986). Archival, unpublished *Spitzer*/MIPS and *Herschel*/PACS images are presented in Figure 16. UW Cen appears as a point source in the *Spitzer*/MIPS images. The higher angular resolution provided by *Herschel*/PACS allows the morphology of the UW Cen CSM to be resolved. The nebula, seen in all three *Herschel*/PACS wavelengths, lies well beyond the reflection nebula (diameter  $\sim 15''$ ) known to exist around UW Cen. The nebula appears spherical at  $100$  and  $160 \mu\text{m}$ .

#### 5.5.2. Radiative Transfer Modeling

The maximum-light UW Cen SED was made by combining archival photometry and spectroscopy with unpublished photometry from *Spitzer*/MIPS and *Herschel*/PACS observations. The SED can be found in Figure 17, and all input photometry in Table 6. The dashed line plotted over the SED represents the best-fit MCRT model from MOCASSIN. Asplund et al. (2000) found from their modeling of spectra against line-blanketed models of stellar atmospheres that the effective temperature of UW Cen is  $\sim 7500$  K. This temperature has been adopted for our MCRT modeling. The distance to UW Cen,  $3.5$  kpc, was calculated from the relation between absolute  $V$ -band magnitude and  $V - I$  color presented in Tisserand et al. (2009). This is a departure from the previous distance calculation of  $5.5$  kpc (Lawson et al. 1990; Clayton et al. 1999), due to underestimating the line-of-sight extinction. This new distance results in an input luminosity of  $7320 L_{\odot}$ .

The UW Cen SED begins to show the influence from CSM after  $2.2 \mu\text{m}$  ( $K$  band). A spherical envelope with inner radius at  $1.55 \times 10^{15}$  cm and outer radius at  $4.50 \times 10^{16}$  cm describes the SED from  $1.6$  to  $\sim 25 \mu\text{m}$ . The dust mass of this envelope is  $2.40 \times 10^{-6} M_{\odot}$  with temperatures ranging from  $\sim 600$  K down to  $\sim 150$  K. This part of the SED is

dominated by the presence of warm dust surrounding the central star. The variability in measurements around  $3 \mu\text{m}$  is due to changes in the amount of warm dust that has recently condensed around UW Cen at the times the observations were taken.

UW Cen’s SED at wavelengths longer than  $\sim 30 \mu\text{m}$  is unlike that of any other known RCB star. A clear second dust component can be seen as the long low-resolution IRS spectrum starts to rise again to a peak around  $70 \mu\text{m}$  before falling again at wavelengths longer than  $100 \mu\text{m}$ . This component was also modeled with a spherical envelope with an inner radius at  $7.00 \times 10^{17}$  cm and outer radius of  $2.50 \times 10^{18}$  cm. The dust mass of this envelope is  $5.14 \times 10^{-3} M_{\odot}$  with temperatures ranging from  $\sim 70$  K down to  $\sim 40$  K.

Analysis of the UW Cen SED was previously presented by both Clayton et al. (1999) and García-Hernández et al. (2011b). Clayton et al. (1999) fit only the optical to MIR with two Planck functions of temperatures  $6000 \pm 500$  and  $650 \pm 50$  K (see their Figure 3). They did not fit wavelengths longer than  $12 \mu\text{m}$  due to the possibility of contamination from IR-bright cirrus clouds along the line of sight to UW Cen. However, they do comment that this contribution can be fit with a Planck function of  $100$  K. A dust mass of  $\sim 6 \times 10^{-4} M_{\odot}$  is derived with a total mass of  $\sim 0.2 M_{\odot}$  assuming a normal gas-to-dust ratio (Clayton et al. 1999).

A four-component fit, stellar + three to account for the CSM contribution, was adopted by García-Hernández et al. (2011b). Similar to Clayton et al. (1999), their fits are only composed of Planck functions. The temperatures of the blackbody fits were  $7500$ ,  $630$ ,  $120$ , and  $50$  K (García-Hernández et al. 2011b). No estimates for the dust masses of any of the components were presented.

## 5.6. V854 Cen

In terms of RCB stars, V854 Cen was discovered relatively recently. In 1986, V854 Cen (NSV 6708) was found to be at  $7.5$  mag when the previous brightest known maximum for this star was at  $9.7$  mag (McNaught & Dawes 1986). Further analysis of archival plates and film by McNaught & Dawes (1986) found that the star appeared as faint as  $15.5$  mag. The peak  $V$ -band brightness of  $7$  mag makes V854 Cen the third brightest RCB star in the entire sky after R CrB and RY Sgr. A star of that brightness would not have been overlooked by the community at large. An examination of archival plates by McNaught (1986) found that V854 Cen had been in decline since at least 1913, which implies that it had been continuously

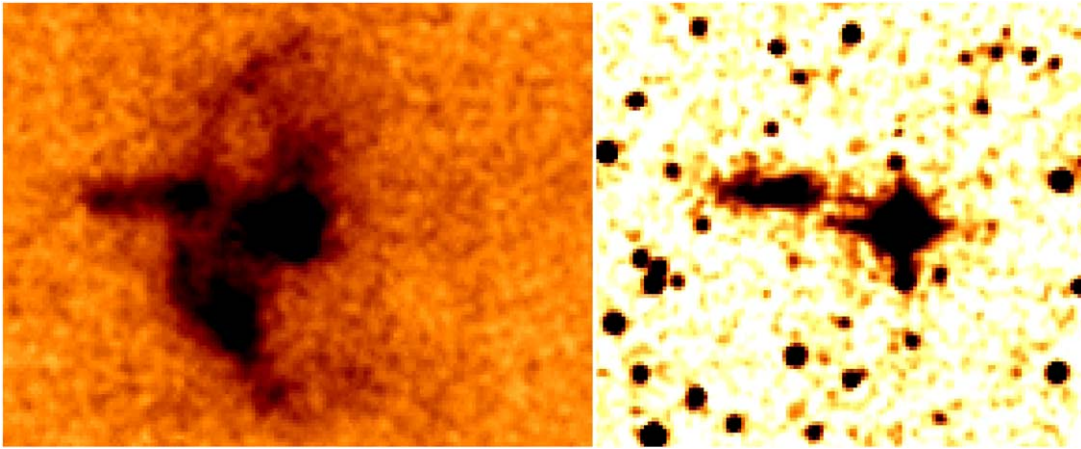


**Figure 14.** Left: zoom-in ( $2''.6 \times 2''.0$ ) of the *Herschel*/PACS  $70 \mu\text{m}$  observation of SU Tau. Right:  $2''.0 \times 2''.0$  field of the 2MASS *J*-band tile containing SU Tau. The bow shock that is prominently seen on the left can be partly seen as a  $0''.5$  vertical line to the east of SU Tau in the 2MASS observation. North is up and east is left.

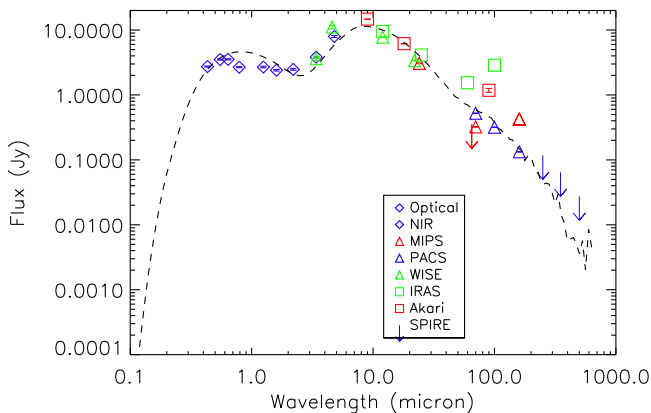


**Figure 15.** Maximum-light SED of SU Tau. Open blue diamonds: *BVRcIcJHKL*; open green triangles: *WISE* (3.4, 4.6, 12.0,  $22.0 \mu\text{m}$ ); open red squares: *AKARI* (9, 18,  $90 \mu\text{m}$ ), a red arrow represents the *AKARI*  $65 \mu\text{m}$  upper limit; open red triangles: *Spitzer*/*MIPS* (24, 70,  $160 \mu\text{m}$ ); open green squares: *IRAS* (12, 25, 60,  $100 \mu\text{m}$ ); open blue triangles: *Herschel*/PACS (70, 100,  $160 \mu\text{m}$ ); blue arrows ( $3\sigma$ ): *Herschel*/SPIRE (250, 350,  $500 \mu\text{m}$ ). The sum of the best-fit MOCASSIN models for the central source, warm, and cold dust shells is represented by the dashed black line.

forming dust along the line of sight during the intervening years.

The abundances of V854 Cen are unusual even for an RCB star. Lawson & Cottrell (1989) found that V854 Cen was much more H-rich than R CrB, and for that matter any other known RCB star. It is one of five RCB stars that are designated “minority” RCB stars (Lambert & Rao 1994). This classification is made primarily based on the lower iron abundances of these RCB stars in relation to the rest of the class. Hema et al. (2012) found evidence that V854 Cen might show enrichment of  $^{13}\text{C}$  from their analysis of high-resolution optical spectroscopy focused on the  $^{12}\text{C}^{13}\text{C}$  Swan band head. They find a  $^{12}\text{C}^{13}\text{C}$  ratio of 16–24, but comment that higher signal-to-noise ratio (S/N) observations are required to better determine the value. This isotope of carbon is found in FF objects like Sakurai’s object, but not in the majority of RCB or HdC stars. It has been examined for any signs of  $^{18}\text{O}$ ,  $^{19}\text{F}$ , or Li, and all have resulted in no detections (Lambert & Rao 1994; Pandey et al. 2008; García-Hernández et al. 2009). Finally, it has been found to have  $\text{C}_{60}$  emission from *Spitzer*/IRS observations (García-Hernández et al. 2011a).

### 5.6.1. Image Inspection

In a similar fashion to MV Sgr, the only FIR observations of V854 Cen are provided by *Spitzer*/*MIPS*. The 24, 70, and  $160 \mu\text{m}$  observations, left to right, respectively, can be found in a three-panel postage stamp displayed in Figure 18. Not much can be said about the morphology of the V854 Cen CSM from these images.

### 5.6.2. Radiative Transfer Modeling

The inputs for the maximum-light SED of V854 Cen are similar to that of MV Sgr. Specifically, this means that archival photometry and spectroscopy are combined with unpublished *Spitzer*/*MIPS* photometry. The SED can be seen in Figure 19 and all input photometry in Table 7. The dashed line represents the best-fit MCRT model from MOCASSIN. An input stellar blackbody with an effective temperature of 6750 K was adopted from atmosphere modeling of Asplund et al. (2000). A distance of 2.28 kpc was determined by assuming an absolute *V*-band magnitude of  $-5$  (Tisserand et al. 2009). This results in an input luminosity of  $11,760 L_{\odot}$ .

Warm dust in the V854 Cen CSM starts to influence the SED after  $1.6 \mu\text{m}$ . This dust component was modeled with an envelope that has an inner radius at  $4.88 \times 10^{14}$  cm and outer radius at  $1.00 \times 10^{16}$  cm. The dust mass of this envelope is  $3.08 \times 10^{-7} M_{\odot}$  with temperatures ranging from  $\sim 1200$  K down to  $\sim 300$  K. A second envelope was also modeled with an inner radius at  $3.45 \times 10^{16}$  cm and extending outward to  $1.00 \times 10^{18}$  cm. The dust mass in this envelope is  $2.60 \times 10^{-5} M_{\odot}$  with temperatures ranging from  $\sim 200$  K down to  $\sim 50$  K.

The maximum-light SED was also used in the blackbody fitting performed by García-Hernández et al. (2011b). A three-component fit (star + two IR excess) was found by García-Hernández et al. to best describe the SED. V854 Cen was fit with a 6750 K blackbody and the two IR excesses with blackbodies of 900 and 140 K (García-Hernández et al. 2011b). The stellar component agrees with the temperature derived by Asplund et al. (1998). The temperatures for the IR excesses fall within the ranges for our two modeled envelopes.

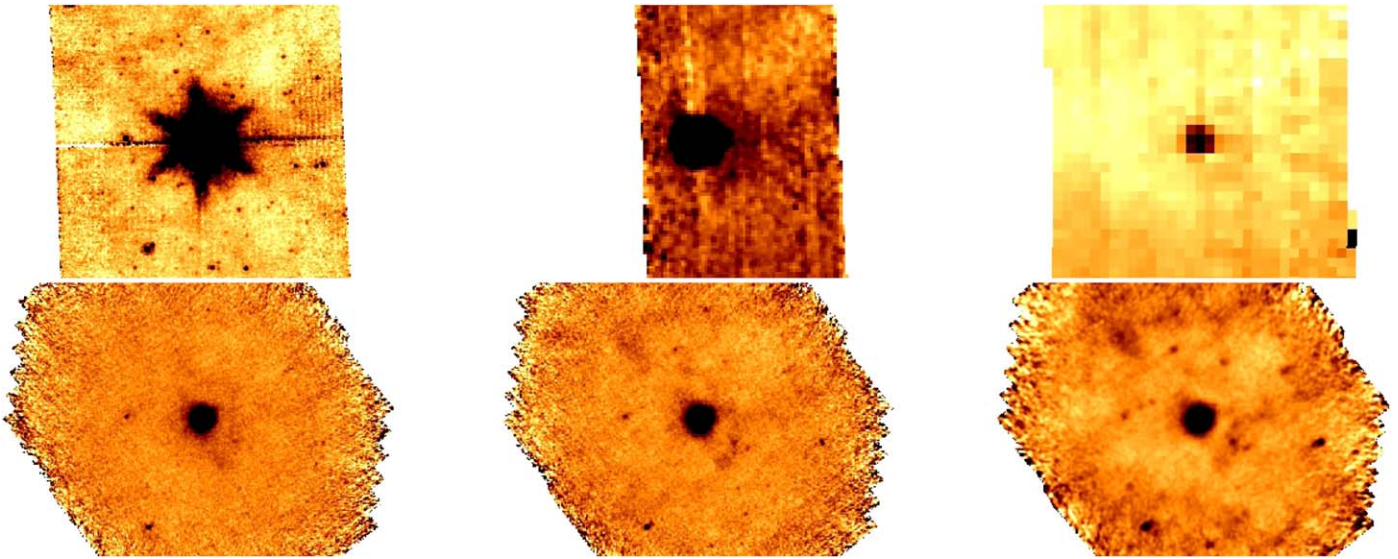


**Figure 16.** Top row: *Spitzer*/MIPS observations of UW Cen at 24, 70, 160  $\mu\text{m}$ , respectively. Bottom row: *Herschel*/PACS observations of UW Cen at 70, 100, and 160  $\mu\text{m}$ , respectively. The fields of view in the *Spitzer* images are all  $8'.0 \times 7'.5$  and in the *Herschel* images are all  $10'.6 \times 7'.5$ . North is up and east is left.

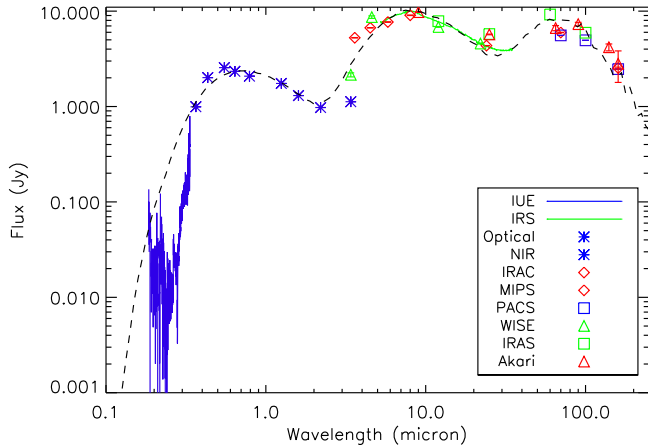


**Figure 17.** Maximum-light SED of UW Cen. Blue line: *IUE* spectrum; blue asterisks: *UBVR<sub>C</sub>JHKL*; open red diamonds: *Spitzer*/IRAC (3.6, 4.5, 5.8, 8.0  $\mu\text{m}$ ) and *Spitzer*/MIPS (24, 70, 160  $\mu\text{m}$ ); open green triangles: *WISE* (3.4, 4.6, 12.0, 22.0  $\mu\text{m}$ ); green line: *Spitzer*/IRS spectrum; open green squares: *IRAS* (12, 25, 60, 100  $\mu\text{m}$ ); open red triangles: *AKARI* (9, 25, 65, 90, 140, and 160  $\mu\text{m}$ ); open blue squares: *Herschel*/PACS (70, 100, 160  $\mu\text{m}$ ). The sum of the best-fit MOCASSIN models for the central source, warm, and cold dust shells is represented by the dashed black line.

## 5.7. V CrA

Changes of at least 1 mag in the brightness of V CrA were first reported by Pickering & Leland (1896). V CrA is also a minority RCB star in addition to having an enrichment of  $^{13}\text{C}$  by the detection of the  $^{12}\text{C}^{13}\text{C}$  Swan band head (Rao & Lambert 2008). This makes it one of three RCB stars to be confirmed to show enrichment of this isotope of carbon. No appreciable level of Li was found to exist in its photosphere (Lambert & Rao 1994). Pandey et al. (2008) made a possible detection of  $^{19}\text{F}$  in the spectrum of V CrA.

### 5.7.1. Image Inspection

*Spitzer*/MIPS, *Herschel*/PACS, and *Herschel*/SPIRE images of V CrA were examined for the presence of diffuse CSM. These images displayed as postage stamps can be found in Figure 20. The improved angular resolution with *Herschel*/PACS allows

accurate detections of V CrA at all three wavelengths. There does appear to be a hint of nebulosity in the north–south direction in the *Herschel*/PACS images, but V CrA appears as a point source in the *Herschel*/SPIRE images.

### 5.7.2. Radiative Transfer Modeling

The V CrA SED was made from available maximum-light photometry and spectroscopy, which were combined with photometry from unpublished *Spitzer*/MIPS, *Herschel*/PACS, and *Herschel*/SPIRE. The photometry can be found in Table 8, while the SED is displayed in Figure 21. The *Spitzer*/MIPS 160  $\mu\text{m}$  and *Herschel*/SPIRE are all  $3\sigma$  upper limits. The dashed line represents the best-fit MCRT model from MOCASSIN. A blackbody with  $T_{\text{eff}} = 6250$  K was adopted from atmosphere modeling by Asplund et al. (2000). A distance of 5.5 kpc was determined by assuming an absolute V-band magnitude of  $-5$  (Tisserand et al. 2009). This results in an input luminosity of  $6550 L_{\odot}$ .

The influence from warm dust in the V CrA CSM starts to become prominent after 1.6  $\mu\text{m}$  (*H* band). This material was modeled by a spherical envelope with inner radius at  $1.70 \times 10^{15}$  cm and outer radius at  $4.90 \times 10^{16}$  cm. The dust mass of this envelope is  $4.00 \times 10^{-6} M_{\odot}$  with temperatures ranging from  $\sim 500$  K down to  $\sim 150$  K.

As with the other RCB stars, the V CrA SED cannot be fit with a single dust envelope. Thus a second envelope was modeled to describe the presence of colder CSM surrounding V CrA. This envelope was modeled with an inner radius at  $1.00 \times 10^{17}$  cm and extending outward to  $1.00 \times 10^{18}$  cm. The dust mass of this envelope is  $5.90 \times 10^{-5} M_{\odot}$  with temperatures ranging from  $\sim 130$  K down to  $\sim 50$  K.

The blackbody fitting to the V CrA maximum-light SED is among the most complex in the sample of García-Hernández et al. (2011b). A fit that includes only optical and *Spitzer* observations was best described by three components (star + two IR excesses), while the fitting of optical, *KLMN*, and *IRAS* 25  $\mu\text{m}$  observations yielded four components (star + three IR excesses; García-Hernández et al. 2011b). V CrA was fit with a 6500 K blackbody in both models, which agrees with the spectroscopic effective temperature (Rao & Lambert 2008) and



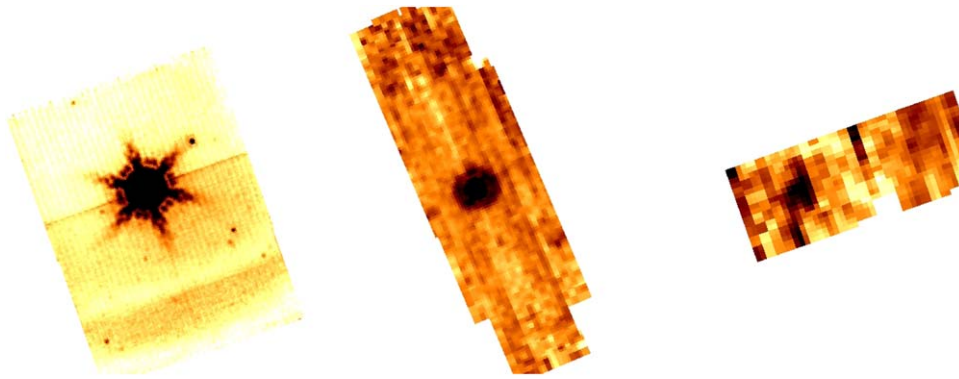


**Figure 18.** *Spitzer*/MIPS observations of V854 Cen at 24, 70, 160  $\mu\text{m}$ , respectively. The fields of view shown (not accounting for white space) are  $6'.0 \times 7'.8$ ,  $3'.4 \times 7'.0$ , and  $5'.4 \times 2'.7$ , respectively. North is up and east is left.

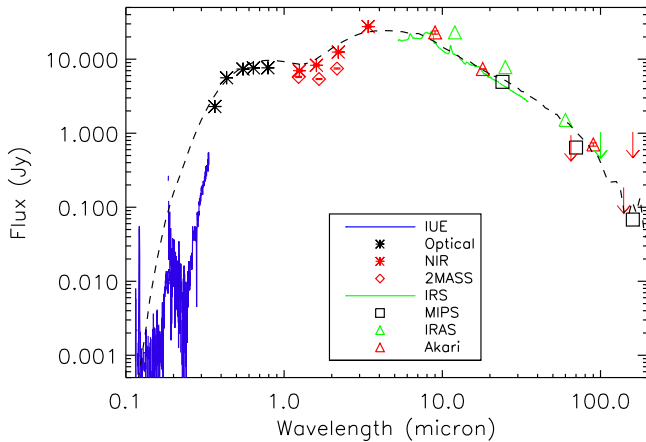


**Figure 19.** Maximum-light SED of V854 Cen. Blue line: *IUE* spectrum; black asterisks:  $UBVR_{\text{C}}I_{\text{C}}$ ; red asterisks:  $JHK_L$ ; open red diamonds: 2MASS  $JHK_S$ ; green line: *Spitzer*/IRS spectrum; open black squares: *Spitzer*/MIPS (24, 70, 160  $\mu\text{m}$ ); open green triangles and arrow ( $3\sigma$ ): *IRAS* (12, 25, 60, 100  $\mu\text{m}$ ); open red triangles and arrow ( $3\sigma$ ): *AKARI* (9, 18, 65, 90, 140, 160  $\mu\text{m}$ ). The sum of the best-fit MOCASSIN models for the central source, warm, and cold dust shells is represented by the dashed black line.

is not very different from the 6250 K (Asplund et al. 2000) used in our modeling. The temperatures in the two IR excess scenarios agree with the ranges determined by the two modeled envelopes. Our MOCASSIN modeling also appears to point to the need for a small reservoir of hot dust close to V CrA to account for the flux values in *MN* and the first two channels of *WISE*.

### 5.8. Sample Properties

The sample presented here is small, but it is of interest to look for trends among the RCB dust shells that have been studied. The results of the MOCASSIN modeling can be found in Table 11. The average properties will also be compared against the HdC star, HD 173409, and the final flash object, V605 Aql.

#### 5.8.1. CSM Morphology

A major surprise of the MCRT SED modeling of the individual RCB stars is that they *all* required the modeling of two discrete, thick dust shells. We employed QuickSAND (see Section 4.2) to better examine the possibility of fitting the SEDs with a single, continuous envelope. QuickSAND models

were performed on the SEDs of R CrB, SU Tau, V854 Cen, and V CrA using the best-fit parameters from our MOCASSIN modeling, but with one continuous shell. These stars were selected because the shapes of their SEDs appear as if they could be fit by one envelope.

This modeling was accomplished by using  $R_{\text{in}}$  of the inner envelope and  $R_{\text{out}}$  of the outer envelope. The output SEDs from the QuickSAND modeling (solid red line) are overplotted on the MOCASSIN best fit (dashed black line) and maximum-light SEDs (squares and solid black lines) in Figures 22–25. The resulting QuickSAND SEDs are close to the MOCASSIN best-fit models, but are overall a poorer fit to the maximum-light SEDs. Additional modeling found that better fits could be achieved by decreasing  $R_{\text{out}}$ . However, this particular constraint is harder to control (see discussion below).

The results of our MCRT agree with those of Nagendra & Leung (1996), who performed analytic modeling and radiative transfer modeling of the R CrB SED. Nagendra & Leung used the available *IRAS* data (Gillett et al. 1986) in their modeling, and they determined that a double shell was the optimal way to fit the SED. Their models were unable to describe emission longer than 60  $\mu\text{m}$  with only one shell. However, Nagendra & Leung did investigate how to model the R CrB SED with a single dusty envelope. They had to greatly increase the contribution from the interstellar radiation field, by a factor of 3–30 (depending on the density profile of the shell) times the normal value, in order to accomplish this (Nagendra & Leung 1996).

We also investigated whether or not the maximum-light SEDs could be described by “thin” dust envelopes. The qualification for an envelope to be “thin” was that  $R_{\text{out}} = 2.0 \times R_{\text{in}}$ . The maximum-light SED of UW Cen was modeled again (see Figure 26). The black dashed line is the same best-fit model as presented earlier, while the red dashed line represents the thin shell model. The modeling with two thin shells has good agreement with the best-fit model up through 10  $\mu\text{m}$ . However, beyond 10  $\mu\text{m}$ , the thin model does not describe the SED well.

The location for  $R_{\text{out}}$  can be calculated from the *Spitzer* or *Herschel* observations. This is derived from the relation between angular diameter and distance (for small angles):  $\theta \approx x/D$ , where  $\theta$  is the angular size of the extended object,  $x$  is the physical size of the object, and  $D$  is the distance to the object. The average ratio of  $R_{\text{out-Outer}}/R_{\text{out-Measured}}$ , excluding UW Cen (see below), is 1.30 with minimum and maximum values of 0.68 (V854 Cen) and 3.31 (RY Sgr), respectively (see Table 11 for the entire sample). Here,  $R_{\text{out-Outer}}$  is the outer

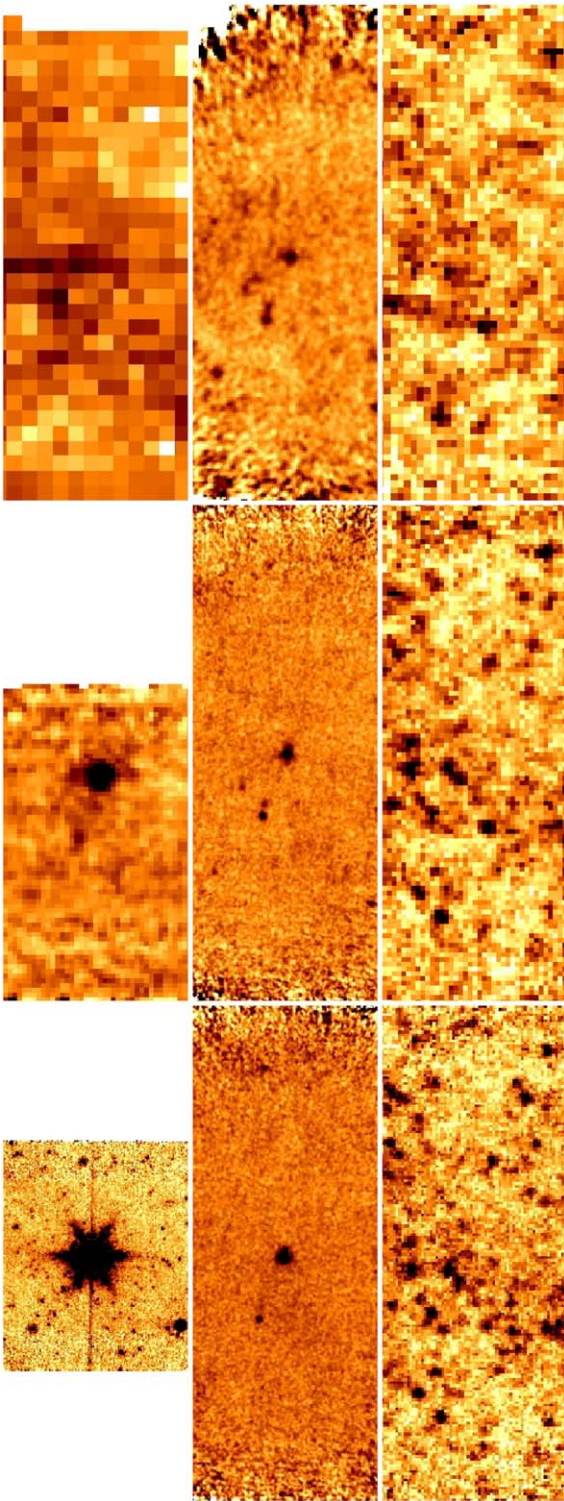


**Figure 20.** First row (starting lower left corner): *Spitzer*/*MIPS* observations of V CrA at 24, 70, 160  $\mu\text{m}$ , respectively. The field of view, ignoring white spaces, displayed at 24  $\mu\text{m}$  is  $8'.5 \times 6'.25$ , at 70  $\mu\text{m}$   $5'.5 \times 3'.2$ , and at 160  $\mu\text{m}$   $8'.0 \times 3'.1$ , and for all three bands is  $25' \times 10'$ . Middle row: *Herschel*/*PACS* observations of V CrA at 70, 100, and 160  $\mu\text{m}$ , respectively. The field of view in all three columns is  $8'.5 \times 3'.2$ . Bottom row: *Herschel*/*SPIRE* observations of V CrA at 250, 350, and 500  $\mu\text{m}$ , respectively. The field of view for all three bands is  $17'.1 \times 6'.3$ . North is left and east is down.

radius of the outer envelope derived from our MCRT modeling, while  $R_{\text{out-Measured}}$  is the value of the same parameter as calculated from the FIR imaging.

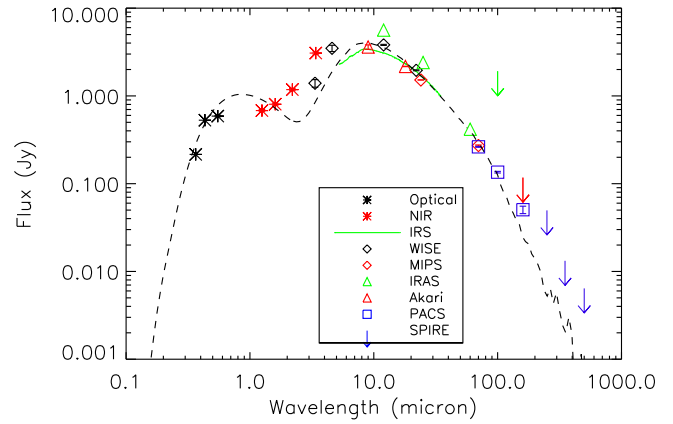


**Figure 21.** Maximum-light SED of V CrA. Black asterisks: *UBV*; red asterisks: *JHK*; open black diamonds: *WISE* (3.4, 4.6, 12.0, 22.0  $\mu\text{m}$ ); green line: *Spitzer*/*IRS* spectrum; open red diamonds: *Spitzer*/*MIPS* (24 and 70  $\mu\text{m}$ ); open green triangles and arrow ( $3\sigma$ ): *IRAS* (12, 25, 60, 100  $\mu\text{m}$ ); open red triangle and arrow ( $3\sigma$ ): *AKARI* (9, 18, 65, 90  $\mu\text{m}$ ); open blue squares: *Herschel*/*PACS* (70, 100, 160  $\mu\text{m}$ ); blue arrows ( $3\sigma$ ): *Herschel*/*SPIRE* (250, 350, 500  $\mu\text{m}$ ). The sum of the best-fit MOCASSIN models for the central source, warm, and cold dust shells is represented by the dashed black line.

**Table 11**  
Derived MOCASSIN Properties and Measured Outer Radii

Star	$R_{\text{in}}$ (cm)	$R_{\text{out}}$ (cm)	$M_{\text{Dust}}$ ( $M_{\odot}$ )	$R_{\text{out-Measured}}$ (cm)
MV Sgr	$3.25 \times 10^{14}$	$9.45 \times 10^{15}$	$7.59 \times 10^{-8}$	$1.03 \times 10^{18}$
	$3.25 \times 10^{16}$	$9.45 \times 10^{17}$	$3.27 \times 10^{-4}$	
R CrB	$1.00 \times 10^{15}$	$3.00 \times 10^{16}$	$9.09 \times 10^{-7}$	$1.23 \times 10^{19}$
	$3.40 \times 10^{17}$	$1.00 \times 10^{19}$	$2.42 \times 10^{-4}$	
RY Sgr	$8.62 \times 10^{14}$	$2.50 \times 10^{16}$	$8.90 \times 10^{-7}$	$1.36 \times 10^{18}$
	$5.15 \times 10^{17}$	$4.50 \times 10^{18}$	$7.25 \times 10^{-4}$	
SU Tau	$2.10 \times 10^{15}$	$4.25 \times 10^{16}$	$2.27 \times 10^{-6}$	$6.91 \times 10^{18}$
	$1.00 \times 10^{18}$	$9.00 \times 10^{18}$	$6.80 \times 10^{-4}$	
UW Cen	$1.55 \times 10^{15}$	$4.50 \times 10^{16}$	$2.40 \times 10^{-6}$	$4.01 \times 10^{17}$
	$7.00 \times 10^{17}$	$2.50 \times 10^{18}$	$5.14 \times 10^{-3}$	
V854 Cen	$4.90 \times 10^{14}$	$1.00 \times 10^{16}$	$3.08 \times 10^{-7}$	$1.48 \times 10^{18}$
	$3.45 \times 10^{16}$	$1.00 \times 10^{18}$	$2.60 \times 10^{-5}$	
V CrA	$1.70 \times 10^{15}$	$4.90 \times 10^{16}$	$4.00 \times 10^{-6}$	$1.39 \times 10^{18}$
	$1.00 \times 10^{17}$	$1.00 \times 10^{18}$	$5.90 \times 10^{-5}$	

The differences between the modeled and measured outer radii are likely due to the uncertainties in the distance to the Galactic RCB stars. The *Gaia* second data release (DR2) was published 2018 April and contained accurate parallaxes for nearly 1.3 billion stars. Six stars, five RCB stars, and one HdC star from our sample were included in the *Gaia* DR2. The distances and  $1\sigma$  uncertainties, accounting for systematics, to these stars are found in Table 1. While *Gaia* represents the largest collection of precise distance measurements, V854 Cen and V CrA are not included in the DR2 release. Further, the uncertainties are still large for MV Sgr and UW Cen. This leaves R CrB, RY Sgr, and SU Tau, for which the distances used for modeling in this paper and the *Gaia* DR2 distances are essentially the same. The largest difference is for SU Tau, which is still within a factor of no more than 2.4 times the upper *Gaia* DR2 uncertainty. Therefore, we have chosen to keep our calculated distances for our modeling. The

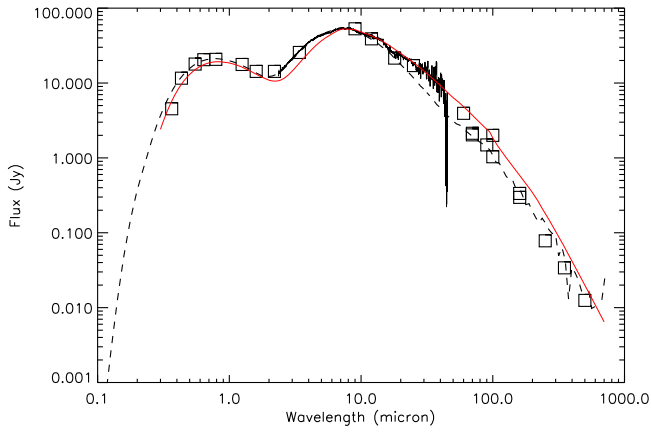


**Figure 22.** Maximum-light SED of R CrB with the same configuration as Figure 8. The best-fit MOCASSIN model is represented by the dashed black line, and the corresponding single-shell model from QuickSAND is represented by the solid red line. The QuickSAND model does not account for the warmest material and overestimates the contribution of the coldest material.

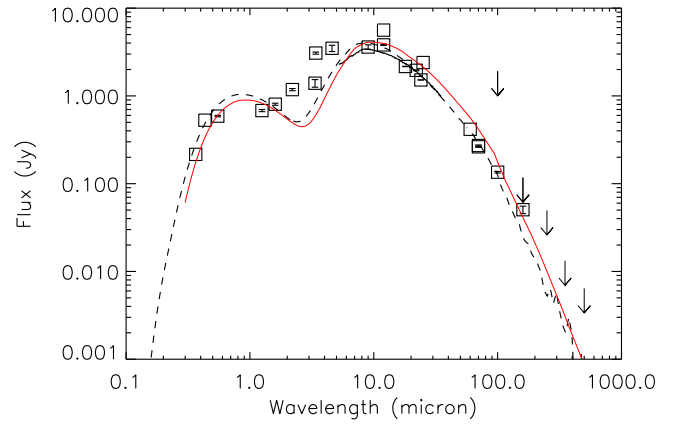


**Figure 25.** Maximum-light SED of V CrA with the same configuration as Figure 21. The best-fit MOCASSIN model is represented by the dashed black line, and the corresponding single-shell model from QuickSAND is represented by the solid red line. The QuickSAND model does not account for the warmest material and overestimates the contribution of the coldest material.

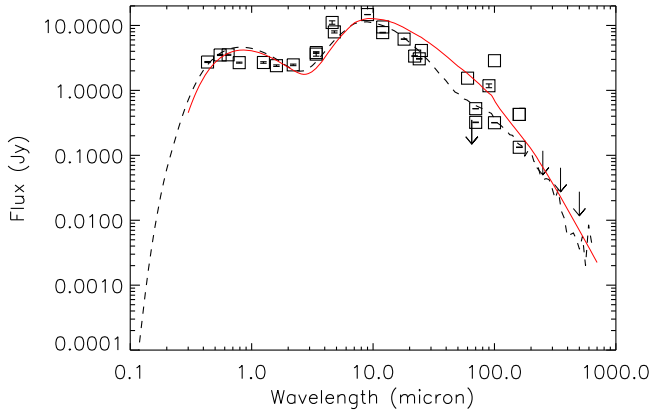


**Figure 23.** Maximum-light SED of SU Tau with the same configuration as Figure 15. The best-fit MOCASSIN model is represented by the dashed black line, and the corresponding single-shell model from QuickSAND is represented by the solid red line. The QuickSAND model does not account for the warmest material and overestimates the contribution of the coldest material.

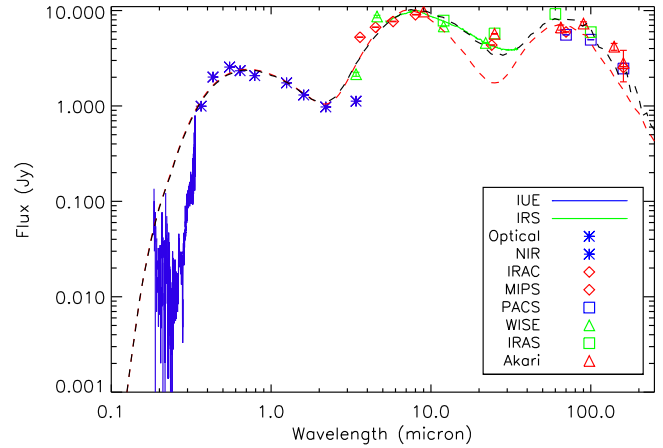


**Figure 26.** Maximum-light SED of UW Cen with the same configuration as Figure 17. The sum of the best-fit MOCASSIN models for the central source, warm, and cold dust shells is still represented by the dashed black line. The MOCASSIN fit for thin shells ( $R_{out} = 2R_{in}$ ) is represented by the red dashed line. The need for thicker shells is apparent in that the SED beyond  $10 \mu\text{m}$  is a poorer match to the thin shell model.

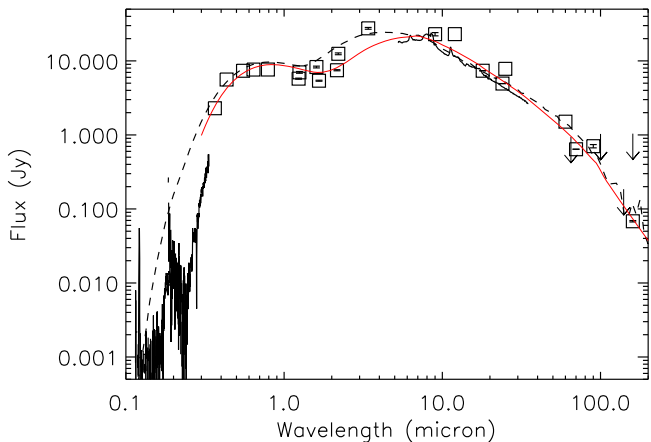


**Figure 24.** Maximum-light SED of V854 Cen with the same configuration as Figure 19. The best-fit MOCASSIN model is represented by the dashed black line, and the corresponding single-shell model from QuickSAND is represented by the solid red line. The QuickSAND model does not account for the warmest material and overestimates the contribution of the coldest material.

uncertainties in our calculated distances are tied to the effective temperatures chosen for our MCRT modeling (Asplund et al. 1997, 2000; De Marco et al. 2002) and that the absolute brightness of the sample RCB stars ranges between  $M_V = -3$  and  $M_V = -5$  (Alcock et al. 2001; Tisserand et al. 2009). These assumptions are not independent of each other. A different choice of temperature would lead to a different absolute brightness, estimated distance, and measured outer radius.

UW Cen is the only case where the outer radius of the inner shell can be calculated because of its reflection nebula, which can be seen at optical wavelengths. The diameter of the reflection nebula has been measured at  $15''$  (Pollacco et al. 1991; Clayton et al. 1999). Clayton et al. (1999) calculated  $R_{out-Measured}$  as being  $6.00 \times 10^{17}$  cm assuming a distance of 5.5 kpc (Lawson et al. 1990). We derived a distance of 3.5 kpc from a higher  $E(B - V)$  than Clayton et al. assumed was present for the line of sight to UW Cen. This corresponds

to the slightly smaller value of  $4.01 \times 10^{17}$  cm for  $R_{\text{out-Measured}}$ . The value of  $R_{\text{out-Measured}}$  derived from the FIR observations is  $2.62 \times 10^{18}$  cm.

First, it is important to note that the best-fit inner envelope lies entirely within  $R_{\text{out-Measured}}$  for the reflection nebula, and that the two values for  $R_{\text{out-Measured}}$  roughly correspond to the modeled values for  $R_{\text{in-Outer}}$  and  $R_{\text{out-Outer}}$ . Here,  $R_{\text{in-Outer}}$  is  $7.00 \times 10^{17}$  cm, which is larger than the derived value but in good agreement with the Clayton et al. (1999) calculation. This indicates that the outer edge of the reflection nebula possibly represents the beginning of the second envelope containing the large reservoir of cold dust predicted by the MCRT. Further, there is excellent agreement ( $<5\%$ ) between the modeled value of  $R_{\text{out-Outer}}$  and the calculation of  $R_{\text{out-Measured}}$  from the FIR observations.

### 5.8.2. Envelope Masses and Decline Activity

The possibility that these large, diffuse shells could have formed during the RCB phase was first examined for R CrB by Montiel et al. (2015). Hence, we searched for a relationship between the physical size and dust mass of the inner and outer envelopes and frequency of declines. It is commonly accepted that the declines are caused when a cloud of carbon dust condenses, along our line of sight, near the central RCB star. Over time, radiation pressure from the central star acts on the cloud, driving it outward into the larger circumstellar environment. Thus, the frequency or length of time an RCB star spends near minimum light is evidence for the formation of fresh dust, at least along the line of sight. Long-term monitoring at  $3.4 \mu\text{m}$  ( $L$  band) is able to follow the creation of new clouds outside the line of sight (i.e., Feast 1997; Feast et al. 1997; Bogdanov et al. 2010). The formation of individual clouds cannot be seen in flux increases, but changes in  $L$ -band brightness by a factor of two over roughly 2 or 3 years indicate higher and lower dust formation activity. The rapid outward expansion of these new dust clouds may produce the large observed envelopes during the RCB phase.

Jurcsik (1996) examined the frequency of declines and the average time between declines in a sample of RCB stars (see her Table 1). All seven of the RCB stars in this paper are in the Jurcsik sample. The minimum inner envelope mass, as determined from our MOCASSIN modeling, is  $7.59 \times 10^{-8} M_{\odot}$  (MV Sgr), while the maximum is  $4.00 \times 10^{-6} M_{\odot}$  (V CrA). MV Sgr is among the least active RCB stars with  $\Delta T_{\text{fades}}$  quoted at 6900 days from two declines in, at the time, 38 years of observations (Jurcsik 1996). On the more active side, UW Cen has had 13 declines in 40 years of observations, which correspond to  $\Delta T_{\text{fades}} = 1100$  days (Jurcsik 1996). The mass of UW Cen’s inner shell is  $2.40 \times 10^{-6} M_{\odot}$ , which is the second largest in our sample. It has also experienced at least two deep decline events since Jurcsik (1996) was published (see the bottom panel of Figure 2).

This implies that either MV Sgr has been producing dust at a rate that is  $\sim 1/10$  of the other RCB stars or we could be viewing it more pole-on. Spectropolarimetric observations of R CrB taken near minimum light suggest that the clouds of dust are more likely to form around the equatorial region of an RCB star than the polar regions (Stanford et al. 1988). Thus, if MV Sgr appears to be more pole-on, it can have a large IR excess from dust production events while only being observed to have a few declines.

We next compared the derived dust masses to the modeled outer radius for the warm and cold shells: see Figure 27. A

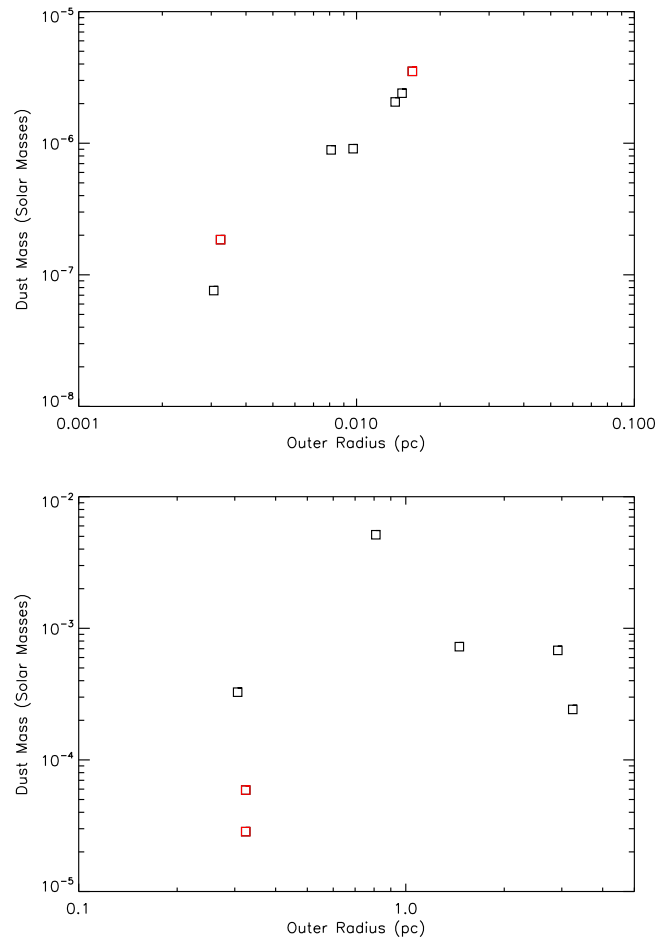


**Figure 27.** Top: plot comparing the derived dust masses to the outer radii of the modeled warm dust envelope for the sample of RCB stars. Bottom: the same as the first plot but for the cold dust envelopes. Majority RCB stars are represented by black squares and minority RCB stars by red squares. The apparent linear trend for the inner envelopes is tied more to the outer radii than a true relationship between dust mass and shell size. No obvious trend arises for the outer envelopes. The minority RCB stars were best fit by smaller, less massive shells than the majority RCB stars for cold envelopes.

power-law trend between the dust mass and outer radius appears to stand out when examining the inner envelopes. However, the origin of this trend arises from the outer radius and volume of the modeled inner envelopes. The envelope with the highest average density is V854 Cen, and the lowest average density is UW Cen. When the same properties are plotted for the outer envelopes, no obvious correlation stands out when this sample is treated as broadly all being RCB stars. However, a slight trend seems to be revealed when individual stars are separated by being either “majority” or “minority” RCB stars. Lambert & Rao (1994) define minority RCB stars as being more iron deficient relative to both other RCB stars and the Sun. In Figure 27, the majority RCB stars are represented by black squares and text, while the minority RCB stars are represented by red squares and text. The warm shells do not reveal any insight, even when divided into majority and minority. The cold shells of the minority RCB stars seem to be both smaller and less massive than the stars of the majority group. Several other chemical factors complicate whether this difference is entirely owed to being minority RCB stars. V854 Cen and V CrA are also both known to be enriched with  $^{13}\text{C}$ , as well as being the two most hydrogen-rich RCB stars.

V854 Cen, in particular, highlights a peculiar case for establishing whether the envelopes are produced during the current RCB phase. The dust masses of the inner and outer envelopes are  $3.08 \times 10^{-7} M_{\odot}$  and  $2.60 \times 10^{-5} M_{\odot}$ , respectively. These values are the second lowest and lowest for our sample. This seems paradoxical since V854 Cen was in decline for nearly half of a century (McNaught 1986). It has also been extremely active since its return to maximum light in the 1980s with nine declines in 9 years of monitoring ( $\Delta T_{\text{fades}} = 370$  days; Jurcsik 1996) and more since then (see the upper panel in Figure 3).

One possible resolution for this discrepancy is that the total time each star has been in the RCB phase is unknown (i.e., what are the relative ages of the different RCB stars to each other?). This issue cannot be resolved by our work, but should V854 Cen be younger than the rest of the RCB stars, then the derived smaller masses of its envelopes would make sense, even with its near half century of decline. Analysis of wind features via the He I  $\lambda 10830$  line, which has been used an indicator of dust expansion velocities (see further below), has found that the velocities seen in V854 Cen can be as strong as  $700 \text{ km s}^{-1}$ , which is a factor of two higher than that measured in other RCB stars (Clayton et al. 2013a).

An important value for this analysis is knowing the true expansion velocity of the dust. Estimates for this motion range from tens to hundreds of  $\text{km s}^{-1}$ . The case for slower moving dust has been attributed to either the natural expansion of a PN shell (Clayton et al. 2011a) or from high-resolution ( $R \sim 30,000$ ), high S/N spectra of scattered star light during deep declines (García-Hernández et al. 2011b, and references therein). Observations of the He I  $\lambda 10830$  line suggest that the dust is rapidly accelerated up to  $400 \text{ km s}^{-1}$  (Clayton et al. 1992a, 2003, 2013a).

Therefore, dust forming at  $2 R_{*}$  ( $170 R_{\odot}$  or  $1.2 \times 10^{13} \text{ cm}$ ) would take 2–20 years to reach  $10^{14}$ – $10^{15} \text{ cm}$ , typical values of  $R_{\text{in}}$  for the inner shell from our RT modeling, at  $20 \text{ km s}^{-1}$ , respectively. Dust moving at higher implied velocities would cover the same distances in 3–9 months. These timescales are much shorter than the lower limit on the lifetime of an RCB star:  $\sim 200$  years from R CrB (Pigott & Englefield 1797). This seems to indicate that at least the inner envelopes could arise from dust ejected during the RCB phase.

The critical issue to resolve is whether or not the continued outward expansion of this dust is also responsible for the observed cold envelopes. Dust moving at  $400 \text{ km s}^{-1}$  would take about  $10^3$ – $10^4$  years to reach anywhere from  $10^{18}$  to  $10^{19} \text{ cm}$ , respectively. It would take an order of magnitude longer for dust moving at  $20 \text{ km s}^{-1}$  to reach those same distances. The slower dust expansion has also led Rao & Nandy (1986) to suggest that these envelopes could be remnant material from the initial red giant phase of these stars. However, in a DD scenario, this phase of stellar evolution would have taken place billions of years before the WD binary would merge.

### 5.8.3. Comparison to an HdC Star and Final Flash Stars

The FF object, V605 Aql, experienced an event in the early 20th century that took it from below the limits of photographic plates ( $m = 15$ ) all the way up to a peak magnitude of 10.2 in 1919 (Wolf 1920). Woods (1921) found that the rise to its maximum brightness was a slow climb over the preceding two years. The languid nature of this outburst originally earned V605 Aql a classification as a slow nova (Lundmark 1921).

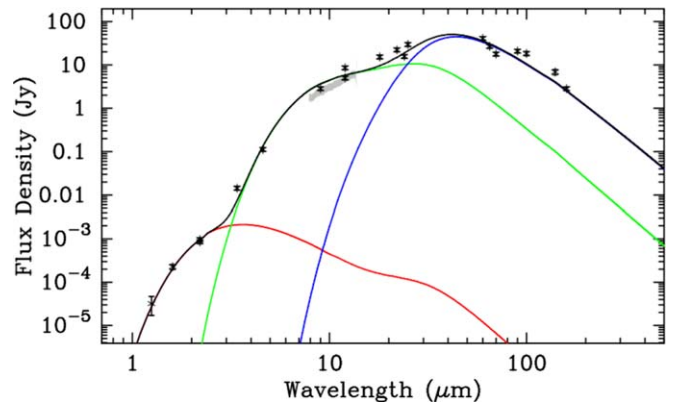


**Figure 28.** V605 Aql SED presented by Clayton et al. (2013b). The black symbols represent photometry from ground-based *JHK* (Hinkle et al. 2008), *WISE*, *AKARI*, *IRAS*, and *Spitzer/MIPS*. The gray line is a spectrum observed with the MID-infrared Interferometric instrument (MIDI) at the Very Large Telescope Interferometer (VLTI). The photometry presented by Clayton et al. is provided in Table 4.9. The red, green, and blue lines are individual fits using the emission curves of amorphous carbon dust with temperatures of 810 K, 235 K, and 75 K, respectively. The black line is the sum of the three fits.

V605 Aql did not spend a significant time at its peak brightness. It began to fade quickly and within a year had fallen below 15th magnitude only to return in 1921, before ultimately fading for good in 1923 (Clayton & De Marco 1997; Clayton et al. 2006, 2013b).

During V605 Aql’s 1921 rebrightening, spectra were acquired at the 0.91 m Crossley telescope (Lundmark 1921). Lundmark discovered that the spectra pointed to V605 Aql as a cool carbon (R0) star and not a classical nova in the late stages of an outburst. This was the last major study of V605 Aql for nearly 50 years. Deep observations obtained independently and published simultaneously by Ford (1971) and van den Bergh (1971) revealed that V605 Aql lies at the center of the old PN Abell 58 (Abell 1966). Further, reanalysis of the Lundmark (1921) spectrum showed that the V605 Aql looked like a cool RCB star (Bidelman 1973; Clayton & De Marco 1997).

Clayton et al. (2013b) presented the modern SED of V605 Aql, which is reproduced in Figure 28. The SED was made from ground-based NIR photometry (Hinkle et al. 2001), ground-based MIR spectroscopy, and IR photometry from several satellites. Optical photometry is not available due to obscuration by the material ejected during the 1919 outburst. In addition to this obscuring dust, a large reservoir of cold dust associated with V605 Aql is immediately apparent since the SED continues to rise to a maximum around  $40 \mu\text{m}$ .

The SED was fit with emission curves of amorphous carbon dust with temperatures and masses as follows: 810 K,  $1.0 \times 10^{-11} M_{\odot}$ ; 235 K,  $9.0 \times 10^{-6} M_{\odot}$ ; 75 K,  $2.0 \times 10^{-3} M_{\odot}$  (Clayton et al. 2013b). These temperatures are in agreement with dust temperatures found in either the first or second envelope of the MCRT for our sample RCB stars. The dust masses calculated by Clayton et al. from the green (235 K) and blue (75 K) components correspond with those derived for the inner and outer shells, respectively, of our RCB sample. However, the evolution of V605 Aql itself has been too rapid when compared to RCB stars. Clayton & De Marco (1997) commented that in 1921 the spectrum of V605 Aql resembled a cool RCB star with  $T_{\text{eff}} \simeq 5000 \text{ K}$ . However, spectra obtained in 2001 revealed the presence of C IV in emission, which indicates that V605 Aql has evolved horizontally back across the HR diagram and is now consistent with  $T_{\text{eff}} \sim 95,000 \text{ K}$  (Clayton et al. 2006), an increase of 90,000 K in

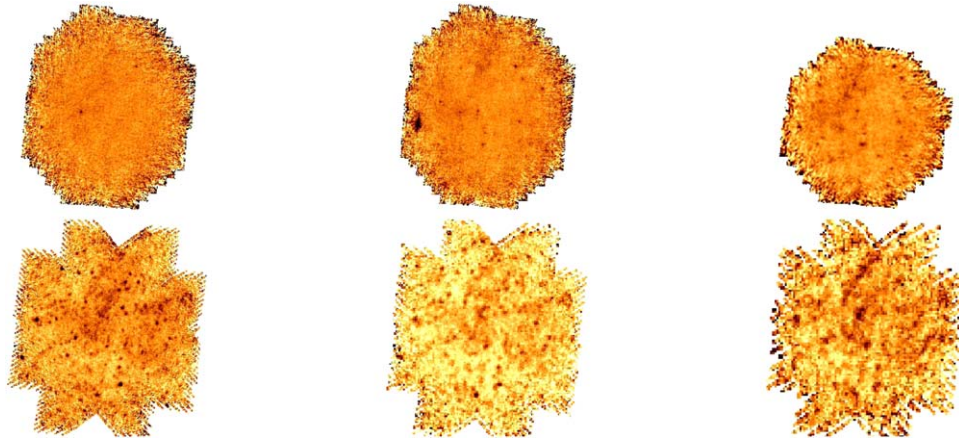


**Figure 29.** Top row: *Herschel*/PACS observations of HD 173409 at 70, 100, and 160  $\mu\text{m}$ , respectively. The 70 and 100  $\mu\text{m}$  fields are both  $9' \times 11'$ , while the 160  $\mu\text{m}$  field is  $9' \times 9'$ . Bottom row: *Herschel*/SPIRE observations of HD 173409 at 250, 350, and 500  $\mu\text{m}$ , respectively. The fields are all  $20' \times 20'$ . The lack of a point source or any nebulosity centered on the position of HD 173409 is consistent with HdC stars having no IR excess.

only 80 years. This change in temperature is more rapid than the minimum lifetime of an RCB star (200 years from R CrB) and from the estimated lifetimes from population synthesis of the RCB stars ( $10^4$ – $10^5$  years; Karakas et al. 2015).

HD 173409 is not an RCB star as normally defined, but is designated as a hydrogen-deficient carbon (HdC) star. These stars are spectroscopically similar to RCB stars, but they do not have the characteristic declines in brightness or display any evidence for IR excess (Warner 1967; Goswami et al. 2010; Tisserand 2012). The spectrum of HD 173409 was first noted as being different from the majority of other stars by Pickering & Fleming (1891) and was identified as being hydrogen-deficient by Bidelman (1953). The HdC stars are also known to have an overabundance of  $^{18}\text{O}$  (Clayton et al. 2005, 2007; García-Hernández et al. 2009, 2010), but the effective temperature of HD 173409 is too high for molecular bands to be detected in its spectrum.

HD 173409 was included in the *Herschel* observing campaign to learn if any cold dust could be surrounding the central star that might have gone previously undetected. This is an excellent test to determine if HdC stars are, in fact, RCB stars that are in an extended period of low decline activity. The *Herschel* PACS and SPIRE observations of HD 173409 can be seen in Figure 29. No nebulosity is visible around HD 173409 in these images.

HD 173409 was in the Tisserand (2012) sample, which examined the early data release by the *WISE* science team. No excess was found in the NIR/MIR from the *WISE* observations. We have constructed the HD 173409 SED from archival photometry and photometry from the ALLWISE catalog. Additionally,  $3\sigma$  upper limits were determined for the *Herschel* observations using a  $30''$ -diameter aperture centered on the position of HD 173409. These upper limits were then included in the HD 173409 SED, which can be found in Figure 30 with a 7000K blackbody overplotted. The photometry that has gone into the HD 173409 SED can be found in Table 10. The absence of an infrared excess in the SED suggests that the CSM of HD 173409 is relatively dust-free. One HdC star, HD 175893, was discovered to have an IR excess from *WISE* photometry (Tisserand 2012). This HdC star could be an example of an RCB star in a phase of low activity in terms of dust production.

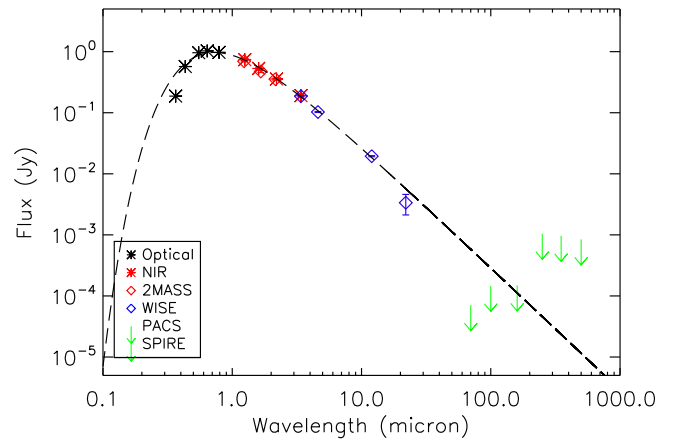


**Figure 30.** HD 173409 SED. Black asterisks: *UBVR<sub>C</sub>*; red asterisks: *JHK<sub>L</sub>*; open blue diamonds: *WISE* (3.4, 4.6, 12.0, 22.0  $\mu\text{m}$ ); green arrows: *Herschel* PACS and SPIRE  $3\sigma$  upper limits.

## 6. Discussion and Conclusions

Montiel et al. (2015) presented and explored three possible interpretations for the origins of the diffuse, dusty nebulosity that surrounds some RCB stars: (1) they are fossil planetary nebulae (PNe), (2) they are remnant material from the merger of a CO and a He WD binary, (3) they have been constructed from dust ejection events during the current RCB phase. We will now examine the results presented here in the context of these three scenarios. The results of the MOCASSIN models are presented in Table 11.

The MCRT modeling of these SEDs suggests the existence of two discrete, concentric spherical shells around each of our sample RCB stars. The construction of these shells during the current RCB phase is critically tied to the number of dust puffs produced, the expansion velocity of the dust puffs, and the lifetime of RCB stars. It has been suggested that during a decline a single puff contains  $\sim 10^{-8} M_{\odot}$  of dust (Clayton et al. 1992a, 2011a). Then,  $\sim 10^{-7} M_{\odot}$  of dust would form per year if a dust puff forms somewhere around the star every 50 days. Thus, an RCB inner envelope would be produced in about 10 years, and it is unlikely that any of the inner shells are the remnant material of a WD merger or fossil PN.

The origin of the outer shells is of greater uncertainty. The data seem to suggest that at some point dust formation ceased and then restarted, or that the inner and outer shells have different origins. For example, the inner shell could be from the RCB phase, and the outer shell could be a fossil PN shell or remnant material from a WD merger. A knowledge of the hydrogen abundance in these shells would help determine whether they are fossil PN shells or not. If the envelopes are fossil PNe, then they should be H-rich. H I measurements at 21 cm of R CrB put lower limits on any hydrogen in its dust shell (Montiel et al. 2015). Assuming R CrB is a typical RCB star, then it is unlikely its dust shell is a fossil PN. Further, recent modeling of the merger rates of WD binaries by Karakas et al. (2015) found that typically the merger will not take place for at least 500 Myr after both stars become WD. This is reinforced by the discovery that the nearby system WD 1242-105 is a binary WD expected to merge in 740 Myr (Debes et al. 2015). After these lengths of time, it is very unlikely that any PN material would still be around an RCB star.

Hydrodynamic modeling of the material that remains following a WD merger suggests that these envelopes would contain  $M_{\text{Dust}} \leq 10^{-6} M_{\odot}$  (Montiel et al. 2015). The mean mass of the outer envelopes in this sample is  $10^{-3} M_{\odot}$ . The least massive envelope (V854 Cen) is implied to contain  $2.60 \times 10^{-5} M_{\odot}$  of dust. This is still an order of magnitude higher than predicted for remnant material from a WD merger.

The velocity of the expanding dust has been estimated as being tens to hundreds of  $\text{km s}^{-1}$ . Slower expansion velocities have been suggested by García-Hernández et al. (2011b, and references therein). Faster outward movement is suggested by the He I  $\lambda 10830$  line, which suggests that the dust is rapidly accelerated up to  $400 \text{ km s}^{-1}$  (Clayton et al. 1992a, 2003, 2013a). The outer envelopes in our sample have implied outer radii that range from  $10^{18} \text{ cm}$  to  $10^{19} \text{ cm}$  (see Table 11). Material at these distances represents the oldest material to be shed by RCB stars. Dust moving with slower velocities,  $20 \text{ km s}^{-1}$ , would take about  $10^4$ – $10^5$  years to reach anywhere from  $10^{18} \text{ cm}$  to  $10^{19} \text{ cm}$ , respectively. These times drop by an order of magnitude if the dust velocities agree more with the results of the He I  $\lambda 10830$  analysis. These timescales are both much longer than we have known about the RCB phenomenon (Pigott & Englefield 1797).

We have compared the observations of the RCB stars to the HdC stars and stars that have been observed to undergo a final flash (FF). HdC stars are essentially spectroscopic twins of RCB stars. HdC stars, however, do not experience decline events and lack any IR excess. The HdC star HD 173409 was observed with both PACS and SPIRE on *Herschel*. No emission associated with HD 173409 was detected in any of the *Herschel* observations. The SED for this star also shows no evidence for any IR excess when fit by a single 7000 K blackbody. Recently, one HdC star, HD 175893, was found to have an IR excess from analysis of *WISE* colors and could either represent a missing link between the two classes of objects or be an RCB star going through an extended period of low dust formation (Tisserand 2012).

The results of our sample were compared to the FF star, V605 Aql, and the findings of Clayton et al. (2013b). Clayton et al. (2013b) presented the SED for V605 Aql, which indicates the presence of  $\sim 10^{-3} M_{\odot}$  of dust associated with its 1919 ejecta. This is a level similar to the dust masses derived from our MOCASSIN modeling for the outer shells. In this scenario, these envelopes would have been created in the recent past.

However, the rapid evolution in the effective temperature of V605 Aql from 5000 to 9500 K in around 80 years (Clayton et al. 2006) has not been found in any RCB star.

The *Herschel* observations of SU Tau with the PACS and SPIRE instruments have led to the discovery of a bow-shock-like structure. This is the first known RCB star to exhibit this type of feature, which represents interactions between the SU Tau CSM and the local interstellar medium (ISM). The bow shock extends between  $30''$  and  $50''$  from the central position of SU Tau, with a brighter feature in the southeast possibly indicating a location where more material is beginning to pile up.

RCB stars are among the most uncommon and bizarre objects discovered in the universe. However, they provide the opportunity to greatly advance our knowledge in areas such as stellar evolution and stellar chemistry. Additional examination of these objects, especially at 21 cm, is needed to determine the origin of the cold, diffuse CSM seen around the RCB stars.

We thank the anonymous referee for feedback that has improved this paper. This work is based in part on observations made with the *Spitzer Space Telescope*, which is operated by the Jet Propulsion Laboratory, California Institute of Technology, under a contract with NASA, and the *Herschel Space Observatory* operated by ESA space with science instruments provided by European-led Principal Investigator consortia and with important participation from NASA. Support for this work was provided by NASA through *Spitzer* contract 1287678 and *Herschel* contract 1485231 issued by JPL/Caltech. D.A.G.H. acknowledges support provided by the Spanish Ministry of Economy and Competitiveness (MINECO) under grant AYA-2017-88254-P.

*Software:* Scanamorphos (version 21.0; Roussel 2013), HIPE (v12; Ott 2010), SExtractor (Bertin & Arnouts 1996), StarFinder (Diolaiti et al. 2000a, 2000b), MOCASSIN (v2.02.70; Ercolano et al. 2003, 2005, 2008), QuickSAND (Sugerman et al. 2012), MIPS DAT (Gordon et al. 2005).

## ORCID iDs

Geoffrey C. Clayton  <https://orcid.org/0000-0002-0141-7436>

N. Kameswara Rao  <https://orcid.org/0000-0002-8414-8541>

M. Matsuura  <https://orcid.org/0000-0002-5529-5593>

## References

- Abell, G. O. 1966, *ApJ*, 144, 259  
 Alcock, C., Allsman, R. A., Alves, D. R., et al. 2001, *ApJ*, 554, 298  
 Asplund, M., Gustafsson, B., Kameswara Rao, N., & Lambert, D. L. 1998, *A&A*, 332, 651  
 Asplund, M., Gustafsson, B., Kiselman, D., & Eriksson, K. 1997, *A&A*, 318, 521  
 Asplund, M., Gustafsson, B., Lambert, D. L., & Rao, N. K. 2000, *A&A*, 353, 287  
 Asplund, M., Lambert, D. L., Kipper, T., Pollacco, D., & Shetrone, M. D. 1999, *A&A*, 343, 507  
 Barnard, F. A. P. 1916, *BHarO*, 617, 1  
 Bertin, E., & Arnouts, S. 1996, *A&AS*, 117, 393  
 Bidelman, W. P. 1953, *ApJ*, 117, 25  
 Bidelman, W. P. 1973, *BAAS*, 5, 442  
 Bogdanov, M. B., Taranova, O. G., & Shenavrin, V. I. 2010, *ARep*, 54, 620  
 Bright, S. N., Chesneau, O., Clayton, G. C., et al. 2011, *MNRAS*, 414, 1195  
 Campbell, L., & Jacchia, L. 1941, *The Story of Variable Stars* (Blakiston, MA: Harvard Monographs)  
 Cannon, A. J., & Pickering, E. C. 1908, *HarCi*, 140, 1  
 Cardelli, J. A., Clayton, G. C., & Mathis, J. S. 1989, *ApJ*, 345, 245

- Clayton, G. C. 1996, *PASP*, **108**, 225
- Clayton, G. C. 2012, *JAVSO*, **40**, 539
- Clayton, G. C., & De Marco, O. 1997, *AJ*, **114**, 2679
- Clayton, G. C., Bond, H. E., Long, L. A., et al. 2013b, *ApJ*, **771**, 130
- Clayton, G. C., De Marco, O., Whitney, B. A., et al. 2011b, *AJ*, **142**, 54
- Clayton, G. C., Geballe, T. R., & Bianchi, L. 2003, *ApJ*, **595**, 412
- Clayton, G. C., Geballe, T. R., Herwig, F., Fryer, C., & Asplund, M. 2007, *ApJ*, **662**, 1220
- Clayton, G. C., Geballe, T. R., & Zhang, W. 2013a, *AJ*, **146**, 23
- Clayton, G. C., Herwig, F., Geballe, T. R., et al. 2005, *ApJL*, **623**, L141
- Clayton, G. C., Kerber, F., Gordon, K. D., et al. 1999, *ApJL*, **517**, L143
- Clayton, G. C., Kerber, F., Pirzkal, N., et al. 2006, *ApJL*, **646**, L69
- Clayton, G. C., Sugerman, B. E. K., Stanford, S. A., et al. 2011a, *ApJ*, **743**, 44
- Clayton, G. C., Whitney, B. A., Stanford, S. A., & Drilling, J. S. 1992a, *ApJ*, **397**, 652
- Clayton, G. C., Whitney, B. A., Stanford, S. A., Drilling, J. S., & Judge, P. G. 1992b, *ApJL*, **384**, L19
- Cohen, M., Wheaton, W. A., & Megeath, S. T. 2003, *AJ*, **126**, 1090
- Cox, N. L. J., Kerschbaum, F., van Marle, A.-J., et al. 2012, *A&A*, **537**, A35
- Cutri, R. M. 2014, *yCat*, **2328**, 0
- Cutri, R. M., Skrutskie, M. F., van Dyk, S., et al. 2003, 2MASS All Sky Catalog of Point Sources (Washington, D.C.: NASA)
- Cutri, R. M., Wright, E. L., Conrow, T., et al. 2012, Explanatory Supplement to the WISE All-Sky Data Release Products, Tech. Rep., 1
- Debes, J. H., Kilic, M., Tremblay, P.-E., et al. 2015, *AJ*, **149**, 176
- Decin, L., Cox, N. L. J., Royer, P., et al. 2012, *A&A*, **548**, A113
- De Marco, O., Clayton, G. C., Herwig, F., et al. 2002, *AJ*, **123**, 3387
- Diolaiti, E., Bendinelli, O., Bonaccini, D., et al. 2000a, in ASP Conf. Ser. 216, *Astronomical Data Analysis Software and Systems IX*, ed. N. Manset, C. Veillet, & D. Crabtree (San Francisco, CA: ASP), 623
- Diolaiti, E., Bendinelli, O., Bonaccini, D., et al. 2000b, *Proc. SPIE*, **4007**, 879
- Drilling, J. S., Schonberner, D., Heber, U., & Lynas-Gray, A. E. 1984, *ApJ*, **278**, 224
- Engelbracht, C. W., Blaylock, M., Su, K. Y. L., et al. 2007, *PASP*, **119**, 994
- Ercolano, B., Barlow, M. J., & Storey, P. J. 2005, *MNRAS*, **362**, 1038
- Ercolano, B., Barlow, M. J., Storey, P. J., & Liu, X.-W. 2003, *MNRAS*, **340**, 1136
- Ercolano, B., Young, P. R., Drake, J. J., & Raymond, J. C. 2008, *ApJS*, **175**, 534
- Fazio, G. G., Hora, J. L., Allen, L. E., et al. 2004, *ApJS*, **154**, 10
- Feast, M. W. 1997, *MNRAS*, **285**, 339
- Feast, M. W., Carter, B. S., Roberts, G., Marang, F., & Catchpole, R. M. 1997, *MNRAS*, **285**, 317
- Ford, H. C. 1971, *ApJ*, **170**, 547
- Fujimoto, M. Y. 1977, *PASJ*, **29**, 331
- Gaposchkin, S. 1952, *AnHar*, **115**, 61
- García-Hernández, D. A., Hinkle, K. H., Lambert, D. L., & Eriksson, K. 2009, *ApJ*, **696**, 1733
- García-Hernández, D. A., Kameswara Rao, N., & Lambert, D. L. 2011a, *ApJ*, **729**, 126
- García-Hernández, D. A., Kameswara Rao, N., & Lambert, D. L. 2011b, *ApJ*, **739**, 37
- García-Hernández, D. A., Lambert, D. L., Kameswara Rao, N., Hinkle, K. H., & Eriksson, K. 2010, *ApJ*, **714**, 144
- García-Hernández, D. A., Rao, N. K., & Lambert, D. L. 2013, *ApJ*, **773**, 107
- Gillett, F. C., Backman, D. E., Beichman, C., & Neugebauer, G. 1986, *ApJ*, **310**, 842
- Goldsmith, M. J., Evans, A., Albinson, J. S., & Bode, M. F. 1990, *MNRAS*, **245**, 119
- Gonzalez, G., Lambert, D. L., Wallerstein, G., et al. 1998, *ApJS*, **114**, 133
- Gordon, K. D., Engelbracht, C. W., Fadda, D., et al. 2007, *PASP*, **119**, 1019
- Gordon, K. D., Rieke, G. H., Engelbracht, C. W., et al. 2005, *PASP*, **117**, 503
- Goswami, A., Karinkuzhi, D., & Shantikumar, N. S. 2010, *ApJL*, **723**, L238
- Griffin, M. J., Abergel, A., Abreu, A., et al. 2010, *A&A*, **518**, L3
- Hecht, J. H., Holm, A. V., Donn, B., & Wu, C.-C. 1984, *ApJ*, **280**, 228
- Helou, G., & Walker, D. W. (ed.) 1988, *Infrared Astronomical Satellite (IRAS) Catalogs and Atlases*, Vol. 7. The Small Scale Structure Catalog (Washington, D.C.: NASA), 0
- Hema, B. P., Pandey, G., & Lambert, D. L. 2012, *ApJ*, **747**, 102
- Herbig, G. H. 1964, *ApJ*, **140**, 1317
- Higdon, S. J. U., Devost, D., Higdon, J. L., et al. 2004, *PASP*, **116**, 975
- Hinkle, K. H., Joyce, R. R., & Hedden, A. 2001, *A&A*, **367**, 250
- Hinkle, K. H., Lebzelter, T., Joyce, R. R., et al. 2008, *A&A*, **479**, 817
- Hoffleit, D. 1958, *AJ*, **63**, 50
- Hoffleit, D. 1959, *AJ*, **64**, 241
- Holm, A. V. 1999, *JAVSO*, **27**, 113
- Houck, J. R., Roellig, T. L., van Cleve, J., et al. 2004, *ApJS*, **154**, 18
- Iben, I., Jr., Tutukov, A. V., & Yungelson, L. R. 1996, *ApJ*, **456**, 750
- Ishihara, D., Onaka, T., Kataya, H., et al. 2010, *A&A*, **514**, A1
- Jeffery, C. S. 1995, *A&A*, **299**, 135
- Jurcsik, J. 1996, *AcA*, **46**, 325
- Karakas, A. I., Ruiter, A. J., & Hampel, M. 2015, *ApJ*, **809**, 184
- Kawada, M., Baba, H., Barthel, P. D., et al. 2007, *PASJ*, **59**, S389
- Keenan, P. C., & Greenstein, J. L. 1963, *Contr. Perk. Obs.*, **2**
- Kilkenny, D., & Whittet, D. C. B. 1984, *MNRAS*, **208**, 25
- Lambert, D. L., & Rao, N. K. 1994, *JApA*, **15**, 47
- Lambert, D. L., Rao, N. K., Pandey, G., & Ivans, I. I. 2001, *ApJ*, **555**, 925
- Landolt, A. U., & Clem, J. L. 2017, *JAVSO*, **45**, 159
- Lawson, W. A., & Cottrell, P. L. 1989, *MNRAS*, **240**, 689
- Lawson, W. A., Cottrell, P. L., Kilmartin, P. M., & Gilmore, A. C. 1990, *MNRAS*, **247**, 91
- Lawson, W. A., Maldoni, M. M., Clayton, G. C., et al. 1999, *AJ*, **117**, 3007
- Leavitt, H. S., & Pickering, E. C. 1906, *HarCi*, **122**, 1
- Lebouteiller, V., Barry, D. J., Spoon, H. W. W., et al. 2011, *ApJS*, **196**, 8
- Lebouteiller, V., Bernard-Salas, J., Sloan, G. C., & Barry, D. J. 2010, *PASP*, **122**, 231
- Leech, K., Kester, D., Shipman, R., et al. 2003, *The ISO Handbook, SWS-The Short Wavelength Spectrometer*, Vol. 5
- Loreta, E. 1935, *AN*, **254**, 151
- Lundmark, K. 1921, *PASP*, **33**, 314
- Marang, F., Kilkenny, D., Menzies, J. W., & Jones, J. H. S. 1990, *SAOAC*, **14**, 1
- Mathis, J. S., Rumpl, W., & Nordsieck, K. H. 1977, *ApJ*, **217**, 425
- McNaught, R. 1986, *IAUC*, **4245**, 2
- McNaught, R. H., & Dawes, G. 1986, *IBVS*, **2928**
- Menzies, J. W., & Feast, M. W. 1997, *MNRAS*, **285**, 358
- Mitronova, S. N., Karachentsev, I. D., Karachentseva, V. E., Jarrett, T. H., & Kudrya, Y. N. 2004, *BSAO*, **57**, 5
- Montiel, E. J., Clayton, G. C., Marcelllo, D. C., & Lockman, F. J. 2015, *AJ*, **150**, 14
- Moshir, M., et al. 1990, *IRAS Faint Source Catalogue*, version 2.0
- Murakami, H., Baba, H., Barthel, P., et al. 2007, *PASJ*, **59**, S369
- Nagendra, K. N., & Leung, C. M. 1996, *MNRAS*, **281**, 1139
- Neugebauer, G., Habing, H. J., van Duinen, R., et al. 1984, *ApJL*, **278**, L1
- O'Keefe, J. A. 1939, *ApJ*, **90**, 294
- Onaka, T., Matsuhara, H., Wada, T., et al. 2007, *PASJ*, **59**, S401
- Ott, S. 2010, in ASP Conf. Ser. 434, *Astronomical Data Analysis Software and Systems XIX*, ed. Y. Mizumoto, K.-I. Morita, & M. Ohishi (San Francisco, CA: ASP), 139
- Pandey, G., Kameswara Rao, N., & Lambert, D. L. 1996, *MNRAS*, **282**, 889
- Pandey, G., Lambert, D. L., & Rao, N. K. 2008, *ApJ*, **674**, 1068
- Pickering, E. C. 1896, *ApJ*, **4**, 138
- Pickering, E. C., & Fleming, W. P. 1891, *AN*, **128**, 11
- Pickering, E. C., & Leland, E. F. 1896, *ApJ*, **4**, 234
- Pigott, E., & Englefield, H. C. 1797, *RSPT*, **87**, 133
- Pilbratt, G. L., Riedinger, J. R., Passvogel, T., et al. 2010, *A&A*, **518**, L1
- Poglitsch, A., Waelkens, C., Geis, N., et al. 2010, *A&A*, **518**, L2
- Pollacco, D. L., Hill, P. W., Houziaux, L., & Manfroid, J. 1991, *MNRAS*, **248**, 1P
- Rao, N. K., & Lambert, D. L. 2008, *MNRAS*, **384**, 477
- Rao, N. K., & Lambert, D. L. 2015, *MNRAS*, **447**, 3664
- Rao, N. K., & Nandy, K. 1986, *MNRAS*, **222**, 357
- Renzini, A. 1979, in *Stars and Star Systems*, Vol. 75 ed. B. E. Westerlund, **155**
- Rieke, G. H., Young, E. T., Engelbracht, C. W., et al. 2004, *ApJS*, **154**, 25
- Robitaille, T. P., Whitney, B. A., Indebetouw, R., Wood, K., & Denzmore, P. 2006, *ApJS*, **167**, 256
- Roussel, H. 2013, *PASP*, **125**, 1126
- Saio, H. 2008, in ASP Conf. Ser. 391, *Hydrogen-Deficient Stars*, ed. A. Werner & T. Rauch (San Francisco, CA: ASP), 69
- Saio, H., & Jeffery, C. S. 2002, *MNRAS*, **333**, 121
- Schaefer, B. E. 1986, *ApJ*, **307**, 644
- Schlafly, E. F., & Finkbeiner, D. P. 2011, *ApJ*, **737**, 103
- Shears, J. 2011, arXiv:1109.4234
- Skrutskie, M. F., Cutri, R. M., Stiening, R., et al. 2006, *AJ*, **131**, 1163
- Sloan, G. C., Kraemer, K. E., Price, S. D., & Shipman, R. F. 2003, *ApJS*, **147**, 379
- Stanford, S. A., Clayton, G. C., Meade, M. R., et al. 1988, *ApJL*, **325**, L9
- Stansberry, J. A., Gordon, K. D., Bhattacharya, B., et al. 2007, *PASP*, **119**, 1038
- Sugerman, B. E. K., Andrews, J. E., Barlow, M. J., et al. 2012, *ApJ*, **749**, 170
- Tisserand, P., Wood, P. R., & Marquette, J. B. 2012, *A&A*, **539**, A51
- Tisserand, P., Wood, P. R., Marquette, J. B., et al. 2009, *A&A*, **501**, 985



- Ueta, T., Speck, A. K., Stencel, R. E., et al. 2006, [ApJL](#), **648**, L39
- van den Bergh, S. 1971, [PASP](#), **83**, 819
- Walker, H. J. 1985, [A&A](#), **152**, 58
- Walker, H. J. 1986, in IAU Coll. 87: Hydrogen Deficient Stars and Related Objects, ed. K. Hunger, D. Schoenberner, & N. Kameswara Rao, **407**
- Walker, H. J., Heinrichsen, I., Richards, P. J., Klaas, U., & Rasmussen, I. L. 1996, [A&A](#), **315**, L249
- Warner, B. 1967, [MNRAS](#), **137**, 119
- Webbink, R. F. 1984, [ApJ](#), **277**, 355
- Whitney, B. A., Wood, K., Bjorkman, J. E., & Cohen, M. 2003a, [ApJ](#), **598**, 1079
- Whitney, B. A., Wood, K., Bjorkman, J. E., & Wolff, M. J. 2003b, [ApJ](#), **591**, 1049
- Wolf, M. 1920, [AN](#), **211**, 119
- Woods, I. 1921, [BHarO](#), **753**, 2
- Woods, I. E. 1928, [BHarO](#), **855**, 22
- Wright, E. L., Eisenhardt, P. R. M., Mainzer, A. K., et al. 2010, [AJ](#), **140**, 1868
- Yamamura, I., Makiuti, S., Ikeda, N., et al. 2009, in AKARI, a Light to Illuminate the Misty Universe, ed. I. Onaka et al. (San Francisco, CA: ASP), **3**
- Young, K., Phillips, T. G., & Knapp, G. R. 1993a, [ApJ](#), **409**, 725
- Young, K., Phillips, T. G., & Knapp, G. R. 1993b, [ApJS](#), **86**, 517